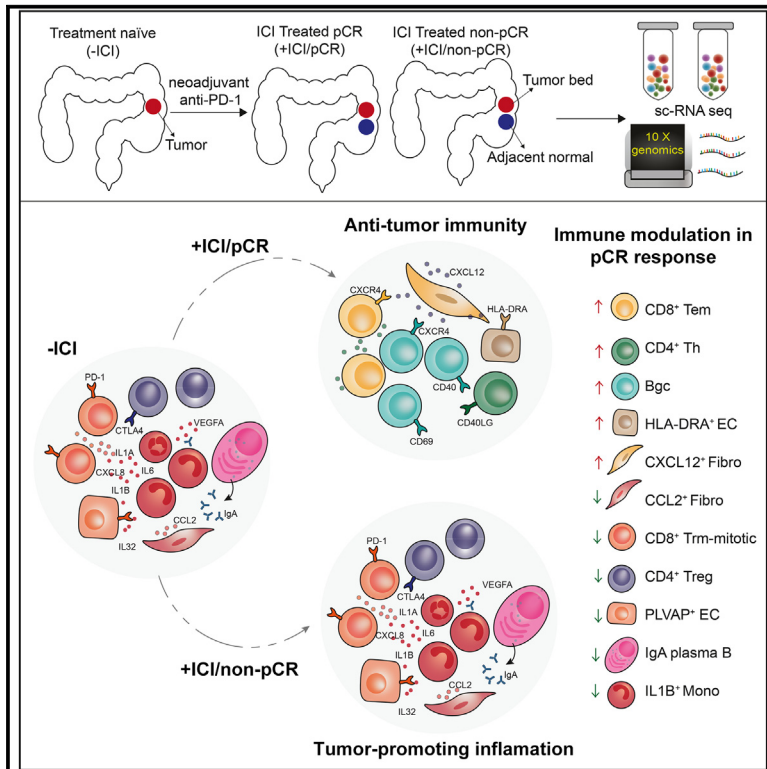


Remodeling of the immune and stromal cell compartment by PD-1 blockade in mismatch repair-deficient colorectal cancer

Graphical abstract



Authors

Jianxia Li, Cheng Wu, Huabin Hu, ..., Yaoxu Chen, Zhi Xie, Yanhong Deng

Correspondence

dengyanh@mail.sysu.edu.cn

In brief

Li et al. use scRNA-seq and multiplex immunohistochemistry to investigate the cellular dynamics in patients with d-MMR/MSI-H CRC treated with neoadjuvant toripalimab, revealing immune and stromal features of complete responders and non-complete responders and highlighting the role of inflammatory conditions in regulating the balance between immune clearance and immune escape.

Highlights

- Immune and stromal cell alterations occur in d-MMR/MSI-H CRC following PD-1 blockade
- Changes in the CD8⁺ T cell cytotoxic and proliferation programs are response-related
- ICI decreases CD4⁺ Tregs and increases CD40⁺ B cells in complete responsive tumors
- Resolution of tumor-promoting inflammation correlates with ICI response

Article

Remodeling of the immune and stromal cell compartment by PD-1 blockade in mismatch repair-deficient colorectal cancer

Jianxia Li,^{1,3,6} Cheng Wu,^{4,6} Huabin Hu,^{1,3,6} Ge Qin,^{1,3,6} Xueqian Wu,^{1,3} Fan Bai,^{1,3} Jianwei Zhang,^{1,3} Yue Cai,^{1,3} Yan Huang,^{2,3} Chao Wang,^{2,3} Jiaqi Yang,⁴ Yizhao Luan,⁴ Zehang Jiang,⁴ Jiayu Ling,^{1,3} Zehua Wu,^{1,3} Yaoxu Chen,⁵ Zhi Xie,⁴ and Yanhong Deng^{1,3,7,*}

¹Department of Medical Oncology, Department of General Surgery, The Sixth Affiliated Hospital, Sun Yat-sen University, Guangzhou 510655, China

²Department of Pathology, Department of General Surgery, The Sixth Affiliated Hospital, Sun Yat-sen University, Guangzhou 510655, China

³Guangdong Provincial Key Laboratory of Colorectal and Pelvic Floor Disease, The Sixth Affiliated Hospital, Sun Yat-sen University, Guangzhou 510655, China

⁴State Key Laboratory of Ophthalmology, Zhongshan Ophthalmic Center, Sun Yat-sen University, Guangzhou 510627, China

⁵Medical Affairs, 3D Medicines Inc., Shanghai 201114, China

⁶These authors contributed equally

⁷Lead contact

*Correspondence: dengyanh@mail.sysu.edu.cn

<https://doi.org/10.1016/j.ccell.2023.04.011>

SUMMARY

Immune checkpoint inhibitor (ICI) therapy can induce complete responses in mismatch repair-deficient and microsatellite instability-high (d-MMR/MSI-H) colorectal cancers (CRCs). However, the underlying mechanism for pathological complete response (pCR) to immunotherapy has not been completely understood. We utilize single-cell RNA sequencing (scRNA-seq) to investigate the dynamics of immune and stromal cells in 19 patients with d-MMR/MSI-H CRC who received neoadjuvant PD-1 blockade. We found that in tumors with pCR, there is a concerted decrease in CD8⁺ Trm-mitotic, CD4⁺ Tregs, proinflammatory IL1B⁺ Mono and CCL2⁺ Fibroblast following treatment, while the proportions of CD8⁺ Tem, CD4⁺ Th, CD20⁺ B, and HLA-DRA⁺ Endothelial cells increase. Proinflammatory features in the tumor microenvironment mediate the persistence of residual tumors by modulating CD8⁺ T cells and other response-associated immune cell populations. Our study provides valuable resources and biological insights into the mechanism of successful ICI therapy and potential targets for improving treatment efficacy.

INTRODUCTION

Mismatch repair-deficient and microsatellite instability-high (d-MMR/MSI-H) represent a distinct biomarker-defined population of cancers accounting for approximately 15% of all colorectal cancers (CRCs).¹ Of all CRCs, d-MMR/MSI-H CRC is associated with a higher tumor neoantigen load and denser immune cell infiltration than mismatch repair-proficient and microsatellite-stable (pMMR/MSS) tumors,^{2,3} suggesting benefit from immune checkpoint inhibitor (ICI) therapy. ICI treatment targeting the PD-1/PD-L1 pathway is highly effective for first-line treatment in patients with metastatic d-MMR/MSI-H CRC^{4–7} and for neoadjuvant treatment in patients with nonmetastatic d-MMR/MSI-H CRC.^{8–10}

However, challenges remain associated with ICI treatment that need to be addressed in order to improve the efficacy of current treatment regimens, since up to 50% of patients with metastatic d-MMR/MSI-H CRC are resistant to immunotherapy with subsequent progression and disease recurrence.^{5–7} The under-

lying mechanisms of complete response of ICI treatment has not been completely understood, which has hindered the improvement of current therapeutic efficacy and regimens for d-MMR/MSI-H CRC. Emerging evidence from gene expression signatures using bulk RNA sequencing (RNA-seq) and multiple immunofluorescence suggests that the efficacy of ICIs largely depends on the tumor immune microenvironment (TIME). It is reported that the response to PD-1 blockade in d-MMR/MSI-H CRC is not associated with tumor mutation burden but with high clonally expanded T cells.¹¹ In the NICHE study, d-MMR colorectal tumors showed significant increases in CD3⁺ and CD8⁺ T cell infiltration as well as interferon (IFN)- γ scores after ICI treatment.⁸ However, these studies mainly rely on profiling technologies that measure tumors in bulk, which limited their ability to capture cell heterogeneity and explore changes in immune components or cellular interactions comprehensively. Recent advances in single-cell RNA-seq (scRNA-seq) have provided an avenue to explore cell type-specific patterns and interactions in the response to ICI treatment at a cellular resolution.

Single-cell analyses of the TIME in solid tumors, such as breast cancer, melanoma, following immunotherapy have been recently published,^{12–15} but it is not clear how such findings can be applied to the study of immunotherapy in CRC. Particularly, single-cell analysis before and after immunotherapy in CRC have not yet been reported.

Here, we present the first in-depth cellular and molecular analysis of cell populations in patients with d-MMR/MSI-H CRC treated with PD-1 blockade (toripalimab) or toripalimab with the COX-2 inhibitor (celecoxib) from a prospective cohort.⁹ The study aims to uncover the underpinnings of resistance and sensitivity to ICI treatment and to suggest the potential therapeutic targets of ICI treatment for residual tumor patients. We compare the cell type distributions and functional changes before and after ICI exposure in patients who achieved pathological complete response (pCR) to elucidate the mechanism related to successful ICI therapy (–ICI vs. +ICI/pCR). We also analyze the differences in treatment dynamics between pCR and non-pCR response to explore the mechanism of resistance to immunotherapy.

RESULTS

Single-cell expression atlas of neoadjuvant immunotherapy-treated d-MMR/MSI-H CRC

The patient cohorts were from a randomized phase 2 study (NCT03926338) with locally advanced primary invasive d-MMR/MSI-H carcinoma of the colon and rectum treated with toripalimab with or without celecoxib for six cycles before curative surgical resection (PICC study).⁹ We performed scRNA-seq on 40 samples of tumor and adjacent normal tissues from 19 patients to characterize cellular and molecular of immune and stromal cells and dynamics during ICI treatment (Figures 1A and S1B; Table S1). Most of the patients (15 of 19) achieved pCR with no residual tumor after neoadjuvant ICI treatment (Figures S1A and S1B; Table S1). In total, we obtained a high-quality single-cell transcriptome atlas for a total of 155,397 cells from 40 samples (Figures S1C and S1E; STAR Methods). Integration of all the samples for cluster analysis revealed clusters representing six broad cell types, including T/I/NK cells (T cells/innate lymphocytes/NK cells), B cells, myeloid cells, epithelial cells, endothelial cells, and fibroblasts (Figure 1B), which expressed known markers accordingly (Figures S1D and S1F). In tumor and normal samples, immune cells (T/I/NK cells, B cells, and myeloid cells) accounted for a large proportion of total cells (29.70% on average in the –ICI group and 27.60% on average in the +ICI/N group) (Figures 1D and S2A). Massive immune cell infiltration was confirmed by multiplex fluorescence immunohistochemical staining (mIHC) (Figure S2B), which was consistent with previous findings in d-MMR/MSI-H CRC.³

By comparing pretreatment and posttreatment samples, we observed that the frequencies of T/I/NK cells, fibroblasts, and endothelial cells significantly increased in the +ICI/pCR group ($p = 0.030$ for T/I/NK cells, $p = 0.049$ for fibroblasts, $p = 0.004$ for endothelial cells, Wilcoxon test) but not in the +ICI/non-pCR group ($p = 0.635$ for T/I/NK cells, $p = 0.188$ for fibroblasts, $p = 0.945$ for endothelial cells, Wilcoxon test) (Figure 1C), suggesting that T/I/NK cells and stromal cells play important roles in ICI treatment. We further reclustered the broad cell types

separately (STAR Methods) and revealed heterogeneous immune and stromal cell subtypes that exhibited distinct molecular signatures indicative of their unique cellular identities (Figures 1E, S2C–S2G).

ICI-related changes in the CD8 T cell cytotoxicity and proliferation program

It is well known that d-MMR/MSI-H tumors demonstrate high infiltration of cytotoxic CD8⁺ T cells and upregulated expression of multiple immune checkpoint molecules, which is also the reason for their sensitivity to immunotherapy.³ We therefore first focused on the CD8⁺ T clusters, which further categorized into intraepithelial lymphocyte (IEL), mucosal-associated invariant T (MAIT), effector memory (Tem), and two tissue resident memory (TRMs) subsets (Figures 2A and 2B; see Table S2 for marker genes). We first used gene set enrichment analysis (GSEA) to explore the effect of ICI on overall CD8⁺ T cell transcriptome. It was found that the trends on the distribution of cytotoxic, exhausted, and proliferated gene signature were correlated with ICI treatment; the cytotoxic signature was enriched in the +ICI/pCR group compared with the –ICI group, while the exhausted and proliferated signatures were enriched in the +ICI/non-pCR group compared with the –ICI group (Figure 2F).

We next analyzed the expression of cytotoxic, exhausted, and proliferated genes in CD8⁺ T clusters to explore the key cell type associated with response to ICI. Among these CD8⁺ T clusters, the CD8⁺ Tem (CD8-C3) and CD8⁺ Trm (CD8-C4) subsets expressed granzymes (*GZMB*, *GZMK*, *GZMA*), perforin 1 (*PRF1*), IFN- γ (*IFNG*), and Fas Ligand (*FASLG*), and were enriched in the CD8 cytotoxic gene signature,^{16,17} which was suggestive of effector functions (Figures 2C and 2E). CD8⁺ Trm (CD8-C4) and CD8⁺ Trm-mitotic (CD8-C5) cells expressed markers of co-inhibitory receptors (*PDCD1*, *LAG3*, *TIGIT*, *HAVCR2*) and exhaustion (*TOX*, *ENTPD1*, *BATF*, *PRDM1*), and were enriched in the CD8 exhaustion signature (Figures 2C and 2E). Further analysis found that CD8⁺ Tem cells showed profound similarities to previously published CD8⁺ T effector memory cells^{18,19} (Figures 2E and S3A), while CD8⁺ Trm (CD8-C4) and CD8⁺ Trm-mitotic (CD8-C5) cells showed features consistent with human TRMs by expressing significantly higher levels of TRMs markers (*ENTPD1* [CD39], *ITGAE*) (Figures 2C and 2G) and enriched TRMs signature^{19–21} (Figures 2E and S3A). These results are consistent with conclusions derived from previous studies that high PD-1 expression is a tissue-residency feature of tumor TRM cells.^{19,21,22}

Having identified candidate subsets of CD8⁺ T cells within d-MMR/MSI-H CRC that bore some similarities to the previously described cytotoxic and exhausted population, we further analyzed changes in frequencies of CD8⁺ T clusters to address whether tumor regression was mainly driven by CD8⁺ T cells, as shown in other cancer types.^{23–25} We observed that ICI treatment induced significant changes in the proportions of CD8⁺ Tem cells ($p = 0.006$, Wilcoxon test) and CD8⁺ Trm-mitotic cells ($p < 0.001$, Wilcoxon test) in pCR response, while the proportion of CD8⁺ Trm cells remained relatively unchanged ($p = 0.648$, Wilcoxon test, Figure 2D). A similar trend was observed in both the anti-PD-1-only regimen- and combination regimen-treated groups compared with the –ICI group (Figure S3B). The distributions of these subsets and their association with pCR suggest

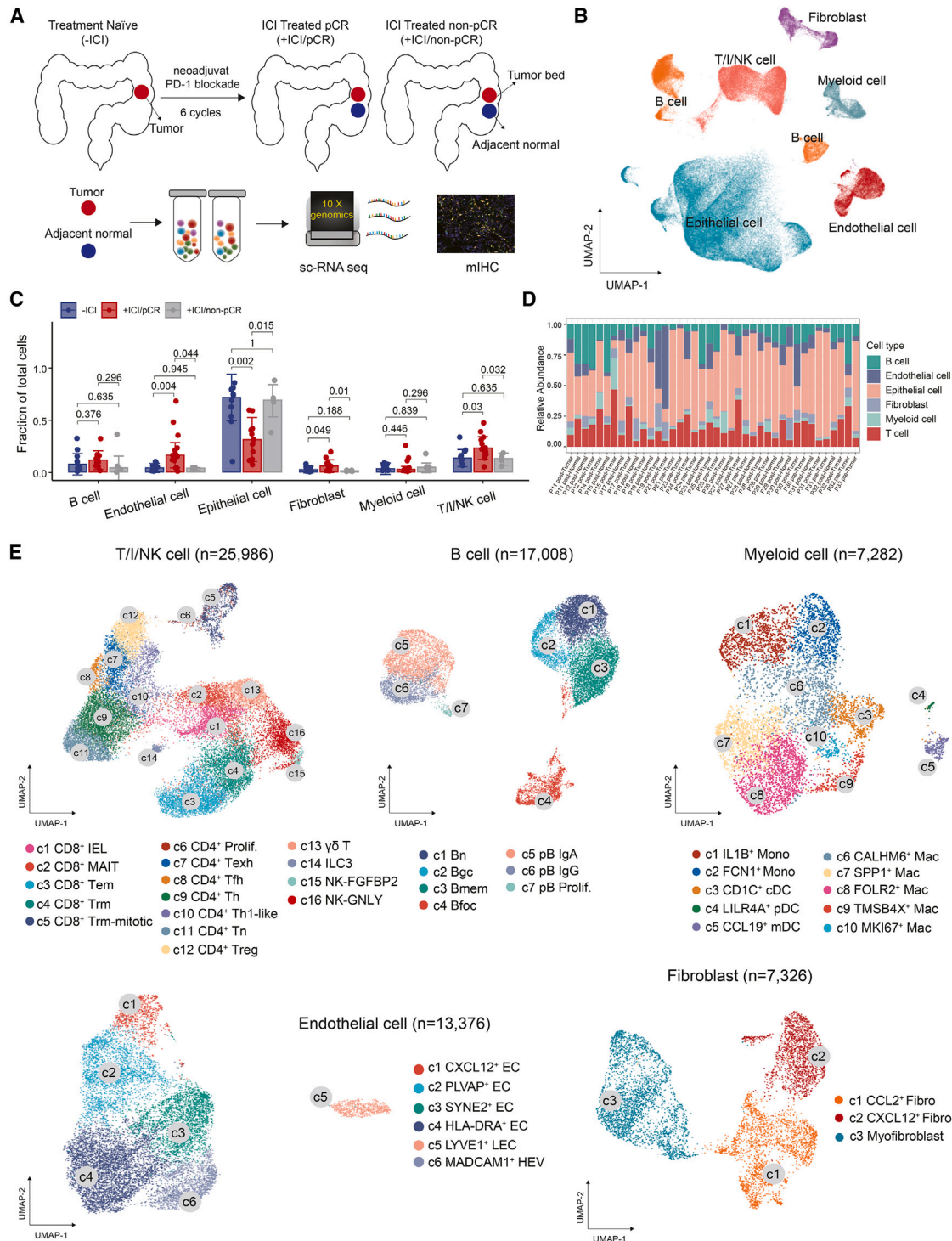


Figure 1. Global analysis of immune and stromal cell populations in d-MMR/MSI-H CRC patients receiving ICI treatment

(A) Overview of the study design.

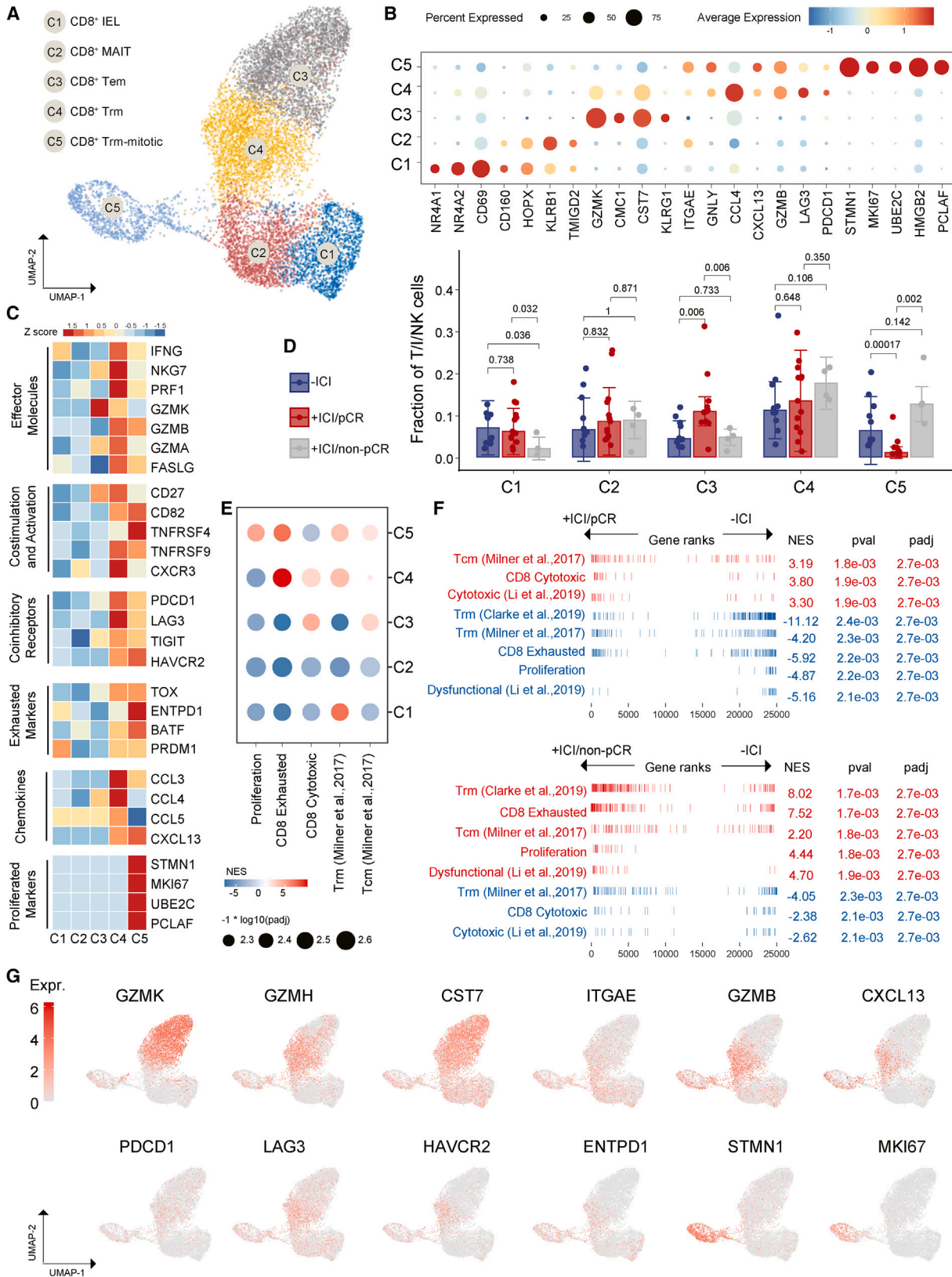
(B) Uniform Manifold Approximation and Projection (UMAP) plot of broad cell types from all samples (n = 40).

(C) Quantification of cell cluster frequency representation among patient groups. The median and interquartile range are shown for each patient group. Two-sided Wilcoxon test.

(D) Cell cluster frequency shown as a fraction of total cells for each sample.

(E) UMAP plots of T//NK cells, B cells, myeloid cells, endothelial cells, and fibroblasts showing transcriptionally distinct clusters.

Also see [Figures S1](#) and [S2](#).



(legend on next page)

the important role of CD8⁺ T cell cytotoxicity and proliferation programs in the neoadjuvant ICI response.

Shared characteristics between ICI-related changes and CD8⁺ Trm transcriptomic alterations

We next sought to address the process of fluctuation in CD8⁺ subset proportions. For pCR tumors, ICI not only increased the proportions of CD8⁺ Tem cells, but also increased antigen presentation processes and characteristic IFN- γ response gene (*HLA-DQA1*, *HLA-DRA*, and *CD74*) expression in CD8⁺ Tem cells (Figure 3A; Table S3) on a per-cell basis. This was consistent with previous clinical observations that PD-1 blockade increased precursor exhausted and effector memory CD8⁺ T cells in human cancer^{23,26} and in mouse models.^{27,28} The expression of HLA-DR genes, which indicate activated CD8⁺ T cell status, was increased mainly in CD8⁺ Tem cells after treatment (Figures 3B and S3E), and the activated HLA-DR⁺ CD8⁺ cells were observed to be improved after treatment via mIHC (Figure S3D). In contrast, CD8⁺ Trm-mitotic cells marked by proliferation marker gene (*MKI67*, *TOP2A*, *STMN1*) dramatically decreased in relative frequencies (Figure 2D) after treatment. The proportion of MKI67⁺ CD8⁺ cells was confirmed to be significantly decreased after treatment in pCR response via mIHC (Figure S3D). Although both CD8⁺ Trm-mitotic and CD8⁺ Trm display CD8 exhaustion features and enriched in exhausted signature, only CD8⁺ Trm-mitotic cells displayed mitotic features with high expression of genes associated with proliferation (Figure 2C), aligning with the previously defined CD8⁺ TRM-like cells actively undergoing cell division in breast cancer.¹⁹ These results indicate that ICI mainly caused the reduction of proliferated subsets of TRMs, not all TRMs.

By calculating the cytotoxicity and exhaustion scores of CD8⁺ T clusters (STAR Methods; Table S3), we found that CD8⁺ Trm cells had higher cytotoxicity and exhaustion scores than CD8⁺ Tem cells but lower exhaustion scores than CD8⁺ Trm-mitotic cells (Figure S3C). Previous study indicated that pre-exhausted and exhausted CD8⁺ T cells form a continuum of cell states with different intensities in proliferating, exhausted, and cytotoxic programs.¹⁶ Together with the evidence that the CD8⁺ Trm cells shared cytotoxic characteristics with CD8⁺ Tem cells and exhausted characteristics with CD8⁺ Trm-mitotic, CD8⁺ Tem, CD8⁺ Trm, and CD8⁺ Trm-mitotic cells indicated the existence of a pool with different degrees of CD8⁺ T cell differentiation in the tumor environment. Trajectory analysis confirmed the potential connections among these three CD8 subsets (Figure 3E).

For transient CD8⁺ Trm cells, antitumor immunity programs were upregulated after ICI treatment, including programs for the antigen receptor-mediated signaling pathway and lymphocyte-mediated immunity (Figure 3C). In addition, we found that *GZMK*, *GZMM*, and IFN- γ response genes (*HLA-DQA2*, *CD74*) were upregulated, while CD8⁺ Trm marker genes (*CXCL13*, *GZMB*, *GNLY*) and immune inhibited receptors (*HAVCR2*, *TNFRSF18*) were downregulated (Figure 3A; Table S3). Overall, the CD8⁺ Tem signature of CD8⁺ Trm cells increased and the CD8⁺ Trm-mitotic signature decreased after ICI treatment (Figure 3D), which indicates that ICI may promote the transformation of CD8⁺ Trm cells to CD8⁺ Tem cells and block the transformation of a portion of CD8⁺ Trm cells into CD8⁺ Trm-mitotic cells, resulting in an increase in CD8⁺ Tem cells and a decrease in CD8⁺ Trm-mitotic cells and eventually resulting in the enhancement of overall antitumor immunity.

CD4⁺ T helper cells and CD20⁺ B cells concertedly expanded in tumors completely responsive to the ICI treatment

Among CD4⁺ T clusters (Figures 4A and 4B), we found a significant decrease in CD4 regulatory cell (Tregs) fraction in pCR samples after ICI treatment ($p = 0.002$, Wilcoxon test, Figure 4D), which was confirmed by mIHC (Figure 4C). This is consistent with a previous study on lung cancer showing that anti-PD-1 decreases Tregs in responsive tumors.²³ Intratumoral Tregs express PD-1 (*PDCD1*) and CTLA-4 (*CTLA4*), which can suppress antitumor immunity.^{29,30} We also found that Treg cells expressed several immune suppressive receptors (IRs), including *TNFRSF18*, *LAG3*, *HAVCR2* (*TIM3*), *CTLA4*, and *TIGIT* (Figures S4B and S4C). Consistently, the fraction of IR-expressed CD4⁺ Tregs decreased after ICI treatment in the pCR group but was more abundant in the non-pCR group (Figure S4D; Table S4). Together, these results indicate that successful ICI treatment reduces the CD4⁺ T cell immunosuppressive program by decreasing Tregs.

In contrast to Tregs, CD4⁺ T helper cells (CD4⁺ Th) marked by high *CD40LG* and *IL7R* gene expression were significantly increased in the pCR group after ICI treatment ($p = 0.008$, Wilcoxon test, Figure 4D). Previous studies have suggested that CD4 helps improve the intrinsic capacity of cytotoxic T lymphocytes (CTLs) to kill target cells and that helpless CTLs express high levels of coinhibitory receptors.³¹ In this study, *CD40LG* was mainly expressed in CD4⁺ T helper subsets, including follicular helper (Tfh), Th1-like, and Th subsets (Figure S4E). We therefore explored the impact of the CD40-CD40LG-helper signature

Figure 2. ICI-related changes in the CD8 T cell cytotoxic and proliferation program

- UMAP plot of CD8⁺ T cell clusters.
 - Dot plots showing marker genes across CD8⁺ T cell clusters. Dot size indicates fraction of expressing cells, colored according to Z score normalized expression levels. See Table S2 for all marker genes.
 - Heatmap of scaled normalized expression for genes in CD8⁺ T cell clusters.
 - Quantification of cell cluster frequency representation among patient groups. The median and interquartile range are shown for each patient group. Two-sided Wilcoxon test.
 - Dot plot of normalized enrichment scores (NES) for gene sets significantly enriched in each CD8⁺ T subset compared with other CD8⁺ T cells. The p values were determined by fast preranked gene set enrichment analysis (GSEA).
 - GSEA enrichment for gene sets in all CD8⁺ T cells comparing pretreatment (–ICI) vs. ICI-treated pCR (+ICI/pCR) and –ICI vs. ICI-treated non-pCR (+ICI/non-pCR). NES, normalize enrichment score. The p values were determined by fast preranked GSEA.
 - UMAP plots showing the expression of selected marker genes in CD8⁺ T cells.
- Also see Figure S3.

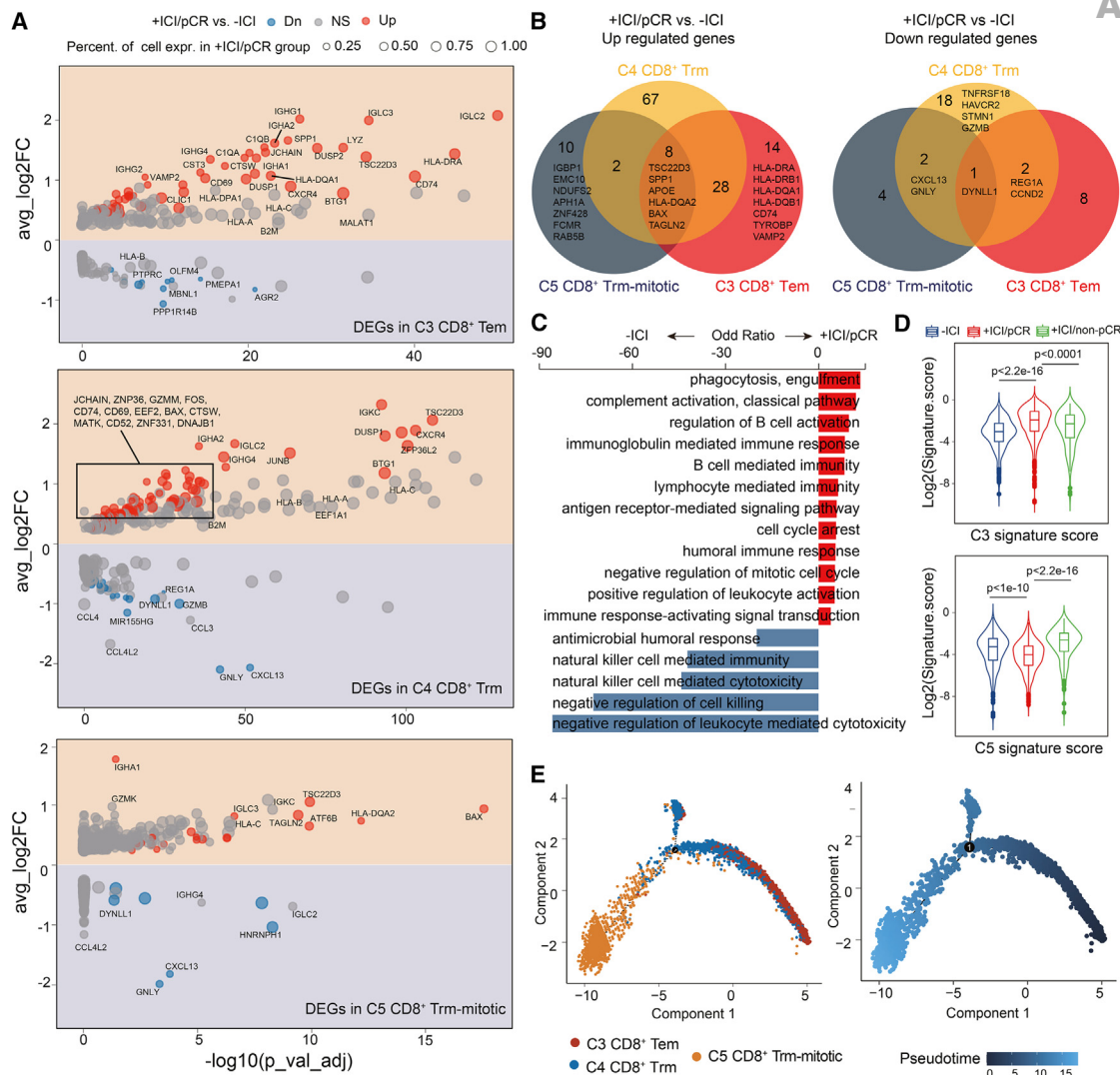


Figure 3. Shared characteristics between ICI-related changes and the CD8⁺ Tm transcriptomic alterations

(A) Differentially expressed genes (DEGs) between the -ICI vs. +ICI/pCR groups among CD8⁺ T clusters. The x axis and y axis values were calculated by the Seurat method. Red points indicate significantly upregulated genes in +ICI/pCR, and blue points indicate significantly downregulated genes in the +ICI/pCR group (STAR Methods).

(B) Venn diagram showing the intersecting and unique DEGs between the -ICI and +ICI/pCR groups in CD8-C3, CD8-C4, and CD8-C5 cells. See Table S3 for all DEGs.

(C) Pathways enriched in CD8⁺ Tm cells in -ICI and +ICI/pCR groups. Hypergeometric test. Benjamini-Hochberg (BH) adjusted p value < 0.05. Odds ratio = Gene Ratio/Background Ratio.

(D) Signature scores computed for the CD8-C4 (CD8⁺ Tm) cells and compared between patient groups with a two-sided Wilcoxon test. Signature scores were defined by the average expression of CD8-C3-specific and CD8-C5-specific marker genes (fold change > 1.5, adjusted p < 0.05, percent expr. > 30%, see Table S2 for marker genes).

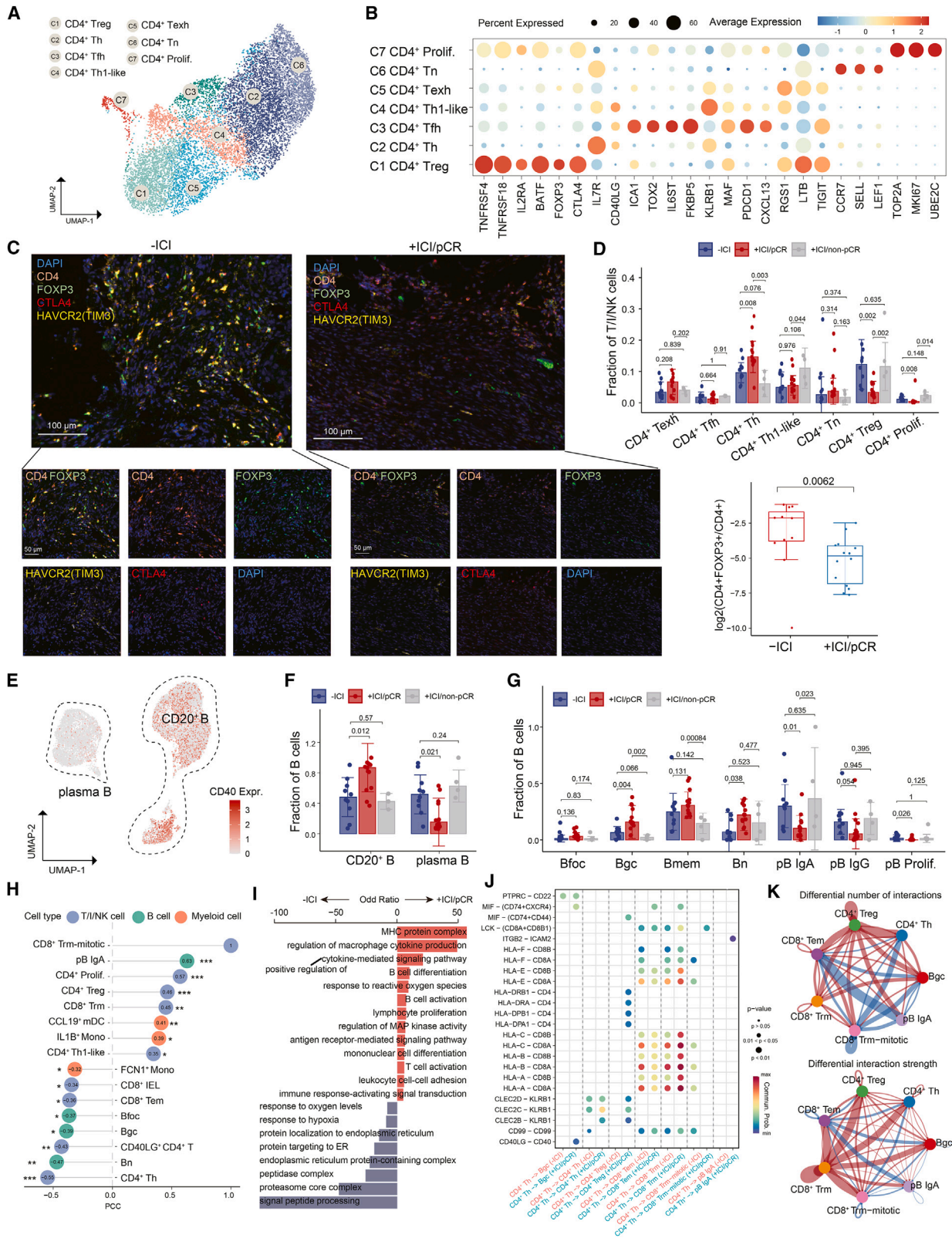
(E) Pseudotime-ordered analysis of CD8⁺ T cell clusters from all samples. CD8⁺ T cell subsets are labeled by color.

Also see Figure S3.

on ICI-induced tumor regression. Overall, CD40LG-positive CD4 cells (CD40LG⁺ CD4⁺ Th) were found to be significantly increased in the pCR group after treatment (Figure S4F; Table S4). Correlation analysis found that CD40LG⁺ CD4⁺ Th cells were negatively correlated with CD8⁺ Tm-mitotic cells (Figure 4H). These results suggest that an effective helper signature expressed by CD40LG⁺ CD4⁺ T helper cells may impair the CD8⁺ T cell exhaustion program.

The interaction of CD40 present on antigen-presenting cells with CD40LG is an essential stimulus for the activation of a vari-

ety of immune and nonimmune cells as a part of humoral and cell-mediated immunity.^{32,33} In this study, CD40 was found to be expressed in both myeloid cells and B cells (Figure S4H). Clustering of B cells showed clear separation of CD20 (MS4A1)⁺ B cells and plasma B cells, with CD40 mainly expressed in CD20⁺ B clusters (Figures S2E and 4E). By comparing the -ICI and +ICI/pCR groups, we found that fraction of CD20⁺ B cells were significantly increased (Figure 4F), in line with their expression of CD40. Increased CD40⁺ CD20⁺ B cells after ICI treatment were validated by mIHC (Figure S4N). Using The



(legend on next page)

Cancer Genome Atlas (TCGA) CRC cohort data, we found that only CD20⁺ B cells were significantly enriched in MSI samples, while plasma B cells showed no group enrichment (Figure S4J). These data suggest that B cells may participate in TIME remodeling caused by PD-1 blockade independent of B cell antibody-driven immunity. By analyzing the transcriptome differences of B cells before and after treatment, we found that the +ICI/pCR group exhibited enrichment for genes related to the antigen receptor-mediated signaling pathway and the T cell activation pathway (Figure 4I). Compared with tumors with low abundance of CD20⁺ B cells, tumors containing high abundance of CD20⁺ B cells had higher CD8⁺ Tem and CD8⁺ Trm cell abundance and lower CD8⁺ Trm-mitotic cell abundance (Figure S4G), suggesting that CD20⁺ B cells are related to CD8⁺ T cell status, which may contribute to the state transition toward pCR.

CD20⁺ B cells were composed of heterogeneous subsets of naive B (Bn), memory B (Bmem), follicular B (Bfoc), and germinal center (Bgc) subsets with distinct transcriptional profiles (Figures 1E and S2D). In these CD40-expressing CD20⁺ B subsets, the most striking increase was observed in Bgc cells ($p = 0.004$, Wilcoxon test) (Figure 4G). Bgc cells are characterized by high expression of genes important for the germinal-center dark zone (*CXCR4*), pronounced germinal center reaction phenotype (*CD69*), and germinal-center selection (*NR4A1*, *NR4A2*) (Figure S2D; Table S2), displaying the characteristics of mature tertiary lymphoid structures (TLS).^{34–36} A study on a preclinical glioma model has demonstrated that systemic delivery of CD40 induces the formation of TLS near meningeal tissue and that the presence of TLS is associated with increased T cell infiltration.³⁷ We also found that a mature TLS signature was highly correlated with CD40-CD40LG expression (Figure S4M), but only the mature TLS signature rather than CD40-CD40LG expression was significantly enriched in MSI tumors (Figure S4L). This connection suggests that CD40-CD40LG may contribute to antitumor immunity by promoting TLS maturation. Next, we studied the relationship between Bgc cells and other immune cells. Bgc cells showed a significant correlation with CD8⁺ T cells, especially CD8⁺ Trm-mitotic cells (Figures 4H and S4K). Cellchat analysis revealed increased number and strength of communications between CD4⁺ Th and Bgc in +ICI/pCR compared with –ICI group (Figure 4K). Stronger

interactions of CD40-CD40LG between Bgc and CD4⁺ Th cells were shown in the +ICI/pCR group (Figure 4J). These results indicate that interaction between CD4⁺ Th and Bgc cells may attribute to antitumor immunity during ICI treatment.

Decreased proinflammatory program in myeloid cells after ICI treatment

Furthermore, re-clustering of 8,469 myeloid cells revealed 10 clusters including macrophages, dendritic cells, and monocytes (Figures 5A and S5A). By comparing the +ICI/pCR and –ICI groups of macrophages and dendritic cells, we found that upregulated genes were associated with phagocytosis, endocytosis, antigen receptor-mediated signaling pathway, and T cell activation (Figure S5F). Notably, we identified two mono-like clusters (IL1B⁺ Mono, FCN1⁺ Mono) based on their high expression of monocyte markers (*FCN1*, *S100A8*, *S100A12*), low expression of both macrophage markers (*CD68*, *CD163*), and HLA genes (Figures 5B and S5A). A previous study revealed the precursor characteristics of FCN1 monocytes.³⁸ However, the function of these monocytes and their involvement with PD-1 blockade-mediated modulation of the TIME have not yet been described. We further analyzed the remodeling of myeloid cell subsets after ICI treatment and found that the proportion of IL1B⁺ Mono cells significantly decreased ($p < 0.001$, Wilcoxon test, Figure 5C). IL1B⁺CD14⁺CD68[–] mono-like cells were confirmed to be infiltrated in d-MMR/MSI-H CRC tumors, with VEGFA cytokines scattered around the cells (Figure 5E). By comparing these cells with other myeloid cells, we observed that IL1B⁺ Mono cells showed the characteristics of inflammatory monocytes by highly expressing the proinflammatory factors *IL6*, *IL1A*, *IL* and the neutrophil chemokines *CXCL8*, *CXCL2*, *CXCL1*, *CCL2*, and *CCL4* (Figure 5D). Inflammation is known to be correlated with cancer development and its response to therapy.³⁹ GSEA showed that differentially expressed genes of IL1B⁺ Mono cells were significantly enriched in the positive regulation of the epithelial-mesenchymal transformation pathway, suggesting the tumor-promoting function of IL1B⁺ Mono cells (Figure S5E).

IL1B⁺ Mono cells remaining after therapy displayed decreased proinflammatory factors than the pretreatment population, including *IL1B* and *CXCL8* (Figure S5C), suggesting their

Figure 4. CD4⁺ Th and CD20⁺ B cells concertedly expanded after ICI treatment

- (A) UMAP plot of CD4⁺ T cell clusters.
 (B) Dot plots showing marker genes across CD4⁺ T cell clusters. Dot size indicates fraction of expressing cells, colored according to Z score normalized expression levels. See Table S2 for all marker genes.
 (C) Representative images of mIHC staining indicating CD4⁺FOXP3⁺ cells, in –ICI and +ICI/pCR samples. Each dot in the boxplot presents the fraction of cells in each sample based on IHC staining image. Two-sided Wilcoxon test.
 (D) Quantification of cell cluster frequency representation among patient groups. The median and interquartile range are shown for each patient group. Two-sided Wilcoxon test.
 (E) UMAP plots of B cell clusters showing expression of *CD40*.
 (F and G) Quantification of the cell cluster frequency representation among patient groups. The median and interquartile range are shown for each patient group. Two-sided Wilcoxon test.
 (H) Correlations of immune cell subsets with CD8⁺ Trm-mitotic in cellular proportions in d-MMR/MSI-H CRCs, $n = 40$. PCC, Pearson correlation coefficient. * $p < 0.05$, ** $p < 0.01$, *** $p < 0.001$, **** $p < 0.0001$.
 (I) Pathways enriched in B cells in –ICI and +ICI/pCR groups. Hypergeometric test. Benjamini-Hochberg (BH) adjusted p value < 0.05 . Odds ratio = Gene Ratio/Background Ratio.
 (J) Receptor–ligand pairs that differ significantly between –ICI and +ICI/pCR based on CD4⁺ Th and other cell clusters. Dot size indicates p value, colored according to the communication probability of pathways.
 (K) Differences in the number and strength of communications of various cell types between +ICI/pCR and –ICI group. The blue line indicates decreased communications in +ICI/pCR, and the red line indicates increased communications in +ICI/pCR. The thicker the line, the greater the difference. Also see Figure S4.

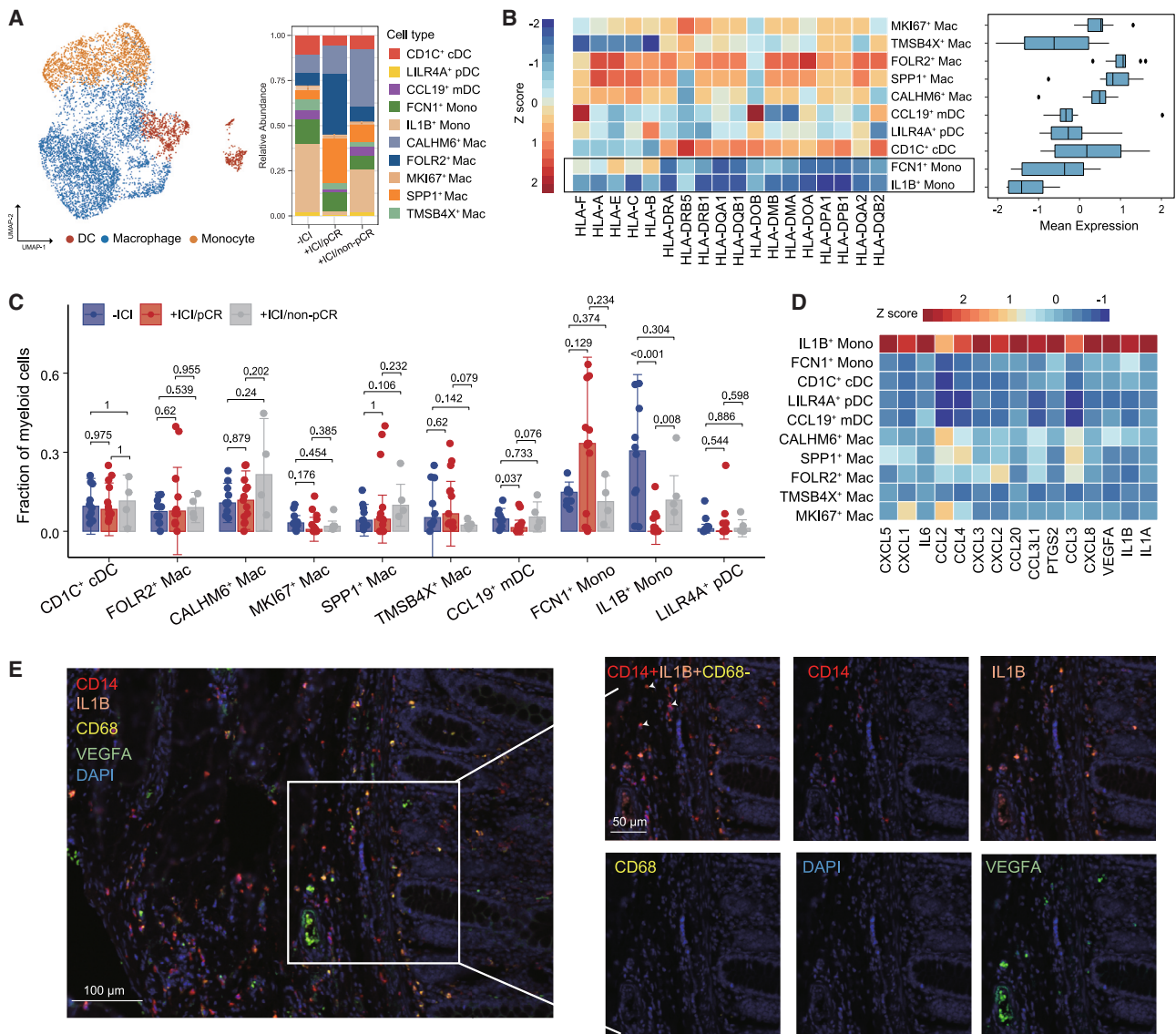


Figure 5. Decreased proinflammatory program in myeloid cells after ICI treatment

(A) UMAP plot of myeloid cells and cell cluster frequency shown as a fraction of total myeloid cells for each group.

(B) Heatmap of scaled normalized expression for HLA-I and HLA-II genes in myeloid cell clusters.

(C) Quantification of cell cluster frequency representation among patient groups. The median and interquartile range are shown for each patient group. Two-sided Wilcoxon test.

(D) Heatmap of scaled normalized expression for proinflammatory genes in myeloid cell clusters.

(E) Representative images of mIHC staining indicating CD68⁻IL1B⁺CD14⁺ cells.

Also see [Figure S5](#).

reduced proinflammatory ability on a per-cell basis. In addition, we also found significant decreases in serum proinflammatory factors after ICI treatment, including *IL1A*, *IL1B*, *IL6*, *CCL20*, and *CXCL2* ([Figure S5D](#)), which further confirmed that ICI in d-MMR/MSI-H CRC modulates the inflammatory program.

Remodeling of stromal cells by ICI treatment

Based on changes in endothelial and fibroblast proportion between -ICI and +ICI/pCR ([Figure 1C](#)) and increased literature highlighting the importance of the cross talk between immune and stromal cells in determining TIME and ICI response,^{40–43}

we next sought to explore the dynamics of stromal cell clusters during ICI treatment. Re-clustering of stromal cells identified three fibroblast subsets and six endothelial cell subsets ([Figures 1E, S2F, and S2G](#); see Marker genes in [Table S2](#)).

As reported in previous study, fibroblasts (Fibro) expressed markers that are colon tissue-specific.⁴⁴ CXCL12⁺ Fibro expressed markers (*DCN*, *SLIT2*, *CXCL12*) of mesenchymal cells distributed throughout the lamina propria, while CCL2⁺ Fibro expressed markers (*F3*, *WNT5A*, *BMP2*, *POSTN*, *HSD17B2*) of a smaller sub-population in close proximity to the epithelial monolayer ([Figures S2G and S6A](#); [Table S2](#)). Myofibroblast

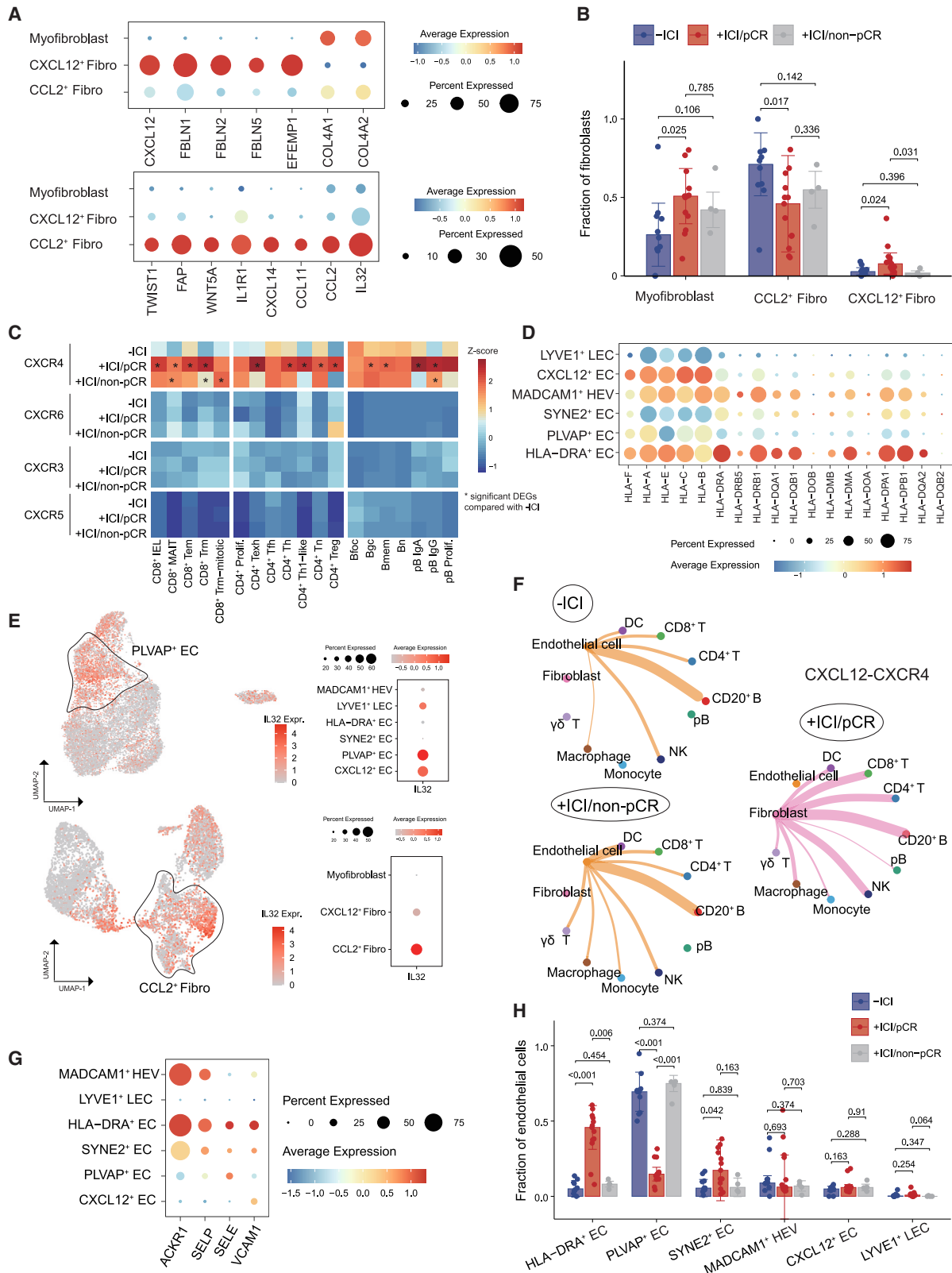


Figure 6. Remodeling of stromal cells by ICI treatment

(A) Dot plots showing selected genes across fibroblast clusters. Dot size indicates fraction of expressing cells, colored according to Z score normalized expression levels.

(legend continued on next page)

and CXCL12⁺ Fibro increased significantly in pCR samples after ICI treatment (Figure 6B). CXCL12⁺ Fibro enriched for elastic fibers (*FBLN1*, *FBLN2*, *FBLN5*, *EFEMP1*), while myofibroblast showed specific expression of sheet collagens (*COL4A1*, *COL4A2*) that are key constituents of the epithelial basement membrane (Figure 6A). In line with increasing CXCL12⁺ Fibro, expressing of *CXCR4* was found upregulated in CD4⁺ T, CD8⁺ T, and B cells after treatment (Figures 6C and S6D). Cell-chat analysis revealed that the interactions between CXCL12 expressed by fibroblast and CXCR4 expressed by lymphocyte populations were enriched specifically in +ICI/pCR (Figures 6F and S6E), indicating CXCL12⁺ Fibro may participate in lymphocyte recruitment via the CXCL12-CXCR4 axis. Although fibroblasts were reported to adopt the CXCL12-CXCR4 axis to restrain T cells in pancreatic cancer,⁴⁵ it has also been shown that CXCL12-producing fibroblasts amass lymphocyte migration.^{46,47}

Among endothelial cells (EC), HLA-DRA⁺ EC increased significantly after treatment in patients who achieved pCR response (Figure 6H). HLA-DRA⁺ EC expressed chemokine receptor D6 (*ACKR1*), *SELP*, *SELE*, and *VCAM1* (Figure 6G), which regulate the migration of leukocytes through the vessel wall.⁴⁸ High expression of major histocompatibility complex class II (MHC-II) surface molecule HLA-DR was found in HLA-DRA⁺ EC cluster (Figure 6D), which allow antigen presentation to CD4⁺ T cells.^{49–51} To investigate global cell-cell interactions in d-MMR/MSI-H CRC, we performed computational modeling by combining scRNA-seq and TCGA bulk RNA-seq dataset analysis, a method previously used in cancer studies.^{38,52,53} We thereby inferred the correlative cell-cell interactions of specific cell types. We observed that HLA-DRA⁺ EC harbored more connections with B cells and CD4⁺ T cells (Figure S6F) than other stromal cells, indicating an important role in assisting immune activation.

In contrast to HLA-DRA⁺ EC and CXCL12⁺ Fibro, PLVAP⁺ EC and CCL2⁺ Fibro significantly decreased after treatment (Figures 6B and 6H). By analyzing characteristics of these two cell clusters, we found they both expressed *IL32* (Figure 6E), which was reported to be involved in proinflammatory and tumor promotion processes.⁵⁴ CCL2⁺ Fibro also displayed characteristics of cancer-associated fibroblasts (*FAP*, *TWIST1*, *WNT5A*)^{55,56} and cytokines that recruit inflammatory monocytes (*CCL2*, *CCL11*) (Figure 6A). In addition, PLVAP⁺ EC highly expressed markers associated with previously reported PLPP3⁺, IGFBP3⁺, and PLVAP⁺ EC (Figure S2F) that located with tumor associated macrophages, Tregs, and tumor epithelial cells

and associated with tumorigenesis.⁵⁷ In summary, these results highlight the important roles of stromal cells in lymphocyte chemotaxis and tumor-promoting inflammation regression during immune remodeling by ICI.

Resolution of pro-tumor inflammation correlated with response

Inflammation has been recognized as being closely involved in the development and progression of malignancies via driving chronic non-resolving inflammation.^{58–60} ICI induced significant decrease of proinflammatory myeloid subsets (IL1B⁺ Mono) and proinflammatory stromal subsets (CCL2⁺ Fibro) (Figures 7A and 7D), suggesting a resolution of inflammation.

CD8 TRMs were reported to attract neutrophils and monocytes by secreting *CCL3* and *CCL4* to trigger innate and adaptive immune responses.^{61,62} In addition, inflammatory stimulation promotes the maturation of TRMs.⁶³ We observed that CD8 TRMs clusters including CD8⁺ Trm and CD8⁺ Trm-mitotic expressed proinflammatory factors (*CCL3*, *CCL4*) and damage-associated molecular patterns (DAMPs) such as *HMGB1* and *HMGB2* (Figure S7A), and have higher inflammatory response scores than other CD8⁺ T cells (Figure S7B). What's more, IL1B⁺ Mono cells were positively correlated with the abundance of CD8⁺ Trm-mitotic cells and, consistently, with the proliferation and exhaustion process (Figure 7C). Consistently, CD8 inflammatory response program was related to the exhaustion and proliferation signature of CD8 TRMs (Figure S7C). These results suggest a positive feedback loop between CD8 TRMs and the inflammatory signaling pathway and that inflammation was associated with the exhaustion program of CD8⁺ T cells.

Next, we sought to explore whether remodeling of CD4⁺ T cells and B cells also has conspicuous overlap with resolution of inflammation. In this study, Tregs have a transcriptional profile similar to inflammation-derived Tregs⁶⁴ characterized by upregulation of both a core Treg (*FOXP3*, *CTLA4*, *TIGIT*) and effector program (*TNFRSF18*, *PRDM1*, *BATF*) (Figure S4C). We observed increased expression of IL1 β receptors (*IL1R1*, *IL1R2*) in Treg cells comparing other CD4⁺ T cells (Figure S7D). Of note, IL1 β receptor positive (IL1R⁺) Tregs had higher Tregs core gene expression than negative Tregs (Figure S7E). These results reveal the association between the inflammatory environment and Tregs, and suggest the possible mechanism of CD4 remodeling during inflammatory resolution in ICI-induced pCR response. For B cells, we observed ICI treatment induced a significant phenotypic switch from plasma B to CD20⁺ B cells in pCR response (Figures 4F and 7A). It has been reported that immunoglobulin

(B) Quantification of cell cluster frequency representation among patient groups. The median and interquartile range are shown for each patient group. Two-sided Wilcoxon test.

(C) Heatmap of scaled normalized expression for *CXCR4*, *CXCR5*, *CXCR6*, and *CXCR3* genes in immune cell clusters. Significant DEGs between –ICI and +ICI/pCR, as well as –ICI and +ICI/non-pCR are marked with asterisks.

(D) Dot plots showing selected genes across endothelial cell clusters. Dot size indicates fraction of expressing cells, colored according to Z score normalized expression levels.

(E) UMAP plots and Dot plots showing *IL32* gene expression across endothelial cell and fibroblast clusters.

(F) Circle plots showing the inferred CXCL12-CXCR4 signaling among cell types under –ICI, +ICI/pCR, and +ICI/non-pCR, respectively.

(G) Dot plots showing selected genes across endothelial cell clusters. Dot size indicates fraction of expressing cells, colored according to Z score normalized expression levels.

(H) Quantification of cell cluster frequency representation among patient groups. The median and interquartile range are shown for each patient group. Two-sided Wilcoxon test.

Also see Figure S6.

(Ig)A-producing and IgG-producing B cells favor tumor growth by contribution to chronic inflammation.^{65–69} In this study, we found a significant decrease of Ig producing B cells after treatment, especially for IgA plasma B cells (Figure 4G).

Taken together, remodeling of immune and stromal cells by ICI in pCR response has striking overlap with pro-tumor inflammatory resolution (Figure 7B). However, unlike pCR, non-pCR did not significantly decrease proinflammatory cells (IL1B⁺ Mono, CCL2⁺ Fibro) after ICI treatment (Figure 7A). Proinflammatory IL1B⁺ Mono cells were enriched in +ICI/non-pCR compared with +ICI/pCR (Figure 7A). Among the ICI efficacy associated cells, inflammatory associated Tregs, CD8⁺ Trm-mitotic, and IgA plasma B cells were also enriched in +ICI/non-pCR compared with +ICI/pCR (Figure 7A). In addition, proinflammatory factors (*IL1A*, *IL1B*, *CCL2/3/4*, *IL6*, *IL32*, *CXCL1*, *CXCL8*, etc.) from myeloid cells, endothelial cells, and fibroblasts were significantly more highly expressed in the +ICI/non-pCR group (Figure S7F). Together, these results suggesting that the mechanism of non-pCR may be a failure of inflammation resolution (Figure 7B). We next sought to elucidate the effects of the inflammatory environment on immune cell populations in an *in vivo* model. We found IL-1 β cytokine treated MC38 mice significantly decreased CD8⁺ T cells and CD40⁺ B cells (Figure S7G). Although proportions of PD-1⁺ exhausted CD8⁺ cells and Treg cells were low, the populations of these cells were potentially increased after IL- β treatment (Figure S7G). These data confirmed correlation between proinflammatory molecules and immunosuppressive TIME and suggested potential targets to improve ICI treatment for d-MMR/MSI-H CRC.

DISCUSSION

We investigated the cellular dynamics during complete responses to ICI treatment in locally advanced d-MMR/MSI-H CRC to ICI treatment. The nonmetastatic neoadjuvant treatment cohort allowed us to clearly observe the specific changes induced by successful immunotherapy. Therefore, we were able to identify the molecular mechanism of immunotherapy in d-MMR/MSI-H CRC and the mechanism of immune escape of residual tumor cells.

In this study, the overall Trm signature was enriched in the non-pCR group (Figure 2F). However, Trm signature has been previously associated with better prognosis in lung cancer²¹ and breast cancer.¹⁹ A possible explanation was that the gene set we use is based on features that distinguish Trm from non-Trm. Therefore, it includes the feature of Trm-mitotic as well, which is related to non-pCR. Our results suggest the importance of identification for Trm subgroups. The finding that proliferating CD8⁺ Trm-mitotic cells decreased after ICI treatment was consistent with the result in a study investigated ICI treatment of melanoma.²⁶ Proliferating CD8⁺ T cells has been reported to be associated with T cell exhaustion in a variety of tumors^{70–72}; however, the mechanism of their formation and maintenance is still unclear. We proposed that the inflammatory environment promotes the transformation from CD8⁺ Trm cells to CD8⁺ Trm-mitotic cells. Consistently, a study performed global analysis of immune cell populations in ICI-induced colitis and found a shift from Trm to proliferating T cells in CD8⁺ T cells.⁷³ Together, these results highlight the association between inflammation and the formation of proliferative CD8⁺ T cells. However,

we do not know the specific correlation between inflammation and processes of proliferation and exhaustion in CD8⁺ T cells. In this study, we used an *in vivo* model and found that IL1 β cytokine increased the proportion of PD-1⁺ exhausted CD8⁺ T cells; however, due to low flow gating of PD-1⁺CD8⁺ cells in the IL1 β -treated group, the association between IL1 β and exhausted CD8⁺ T cells needs to be further validated. Yet we observed a significant decrease of CD8⁺ T cells and CD40⁺ B cells in the IL1 β -treated group, which provides valuable insight on the therapeutic target in immunotherapy.

Despite significant heterogeneity, similar tumor microenvironment remodeling has been observed in a variety of tumors, such as reduction of effector T cells, yet an accumulation of exhausted CD8⁺ T cells and suppressive Tregs, reprogramming of myeloid cells to harbor immunosuppressive phenotypes.^{74,75} Tumors engage common patterns of the immune archetypes and modulate response to ICI.^{76,77} Dynamics of immune cells during ICI treatment in d-MMR/MSI-H CRC found in this study is similar to that of other tumors. For example, in the treatment of non-small cell lung cancer with PD-1 blockade, Liu et al. observed that Tregs decreased only in the responders, and the non-exhausted precursor GZMK⁺ CD8⁺ T cells increased only in the responders.²³ In melanoma treated with ICI therapy (anti-PD-1 and/or anti-CTLA4), Sade et al. found that proliferative CD8⁺ T cells and myeloid cells were enriched in the non-responder group, and B cells rather than plasma cells were enriched in the responder group.²⁶ In advanced renal cell carcinoma, myeloid inflammation is associated with poor overall survival, while the lymphatic system is associated with good overall survival.¹³ Collectively, these results indicate that effective responses to ICIs require non-exhausted T cells as well as depletion of immunosuppressive cells including Tregs and myeloid subsets. Although it has been found that stromal cells can affect the therapeutic effect of ICIs,^{78,79} innovative single-cell approach-based cohort study on the relationship between stromal cells and ICI treatment are relatively lacking. The correlation between stromal cells and the ICI therapeutic effect mentioned in this study provides deeper insights into the functional states and dynamics of stromal cells.

Although we have observed the similarity of tumor immune remodeling in some solid tumors and the importance of relieving the immunosuppressive effect on the response to immunotherapy, it may not be applicable to other diseases called "cold" tumors. While these diseases have not been approved for immunotherapy, relevant research is lacking. These tumors lack immune cell infiltration, and inflammatory response might be needed to recruit immune cells and trigger immune response either by ICI or conventional chemotherapeutic agents and radiation therapy.³⁹ Increased treatment efficacy provided by blocking inflammatory signaling pathways (such as IL-1 β , IL-6, COX2/PGE2) may be more likely to occur in "hot" tumors. In this study, we concluded that non-pCR samples displayed higher expression of proinflammatory factors compared with pCR samples. However, frequencies of IL1B⁺CD14⁺CD68⁻ were compared between pCR and non-pCR samples according to mIHC staining. It may be due to a small sample size in the validation cohort, or the sub-optimal combination of markers that defined IL1B⁺ Mono cells. Future study is needed to validate the association in a larger cohort and optimize the detection methods for the key inflammatory factors and their source cells.

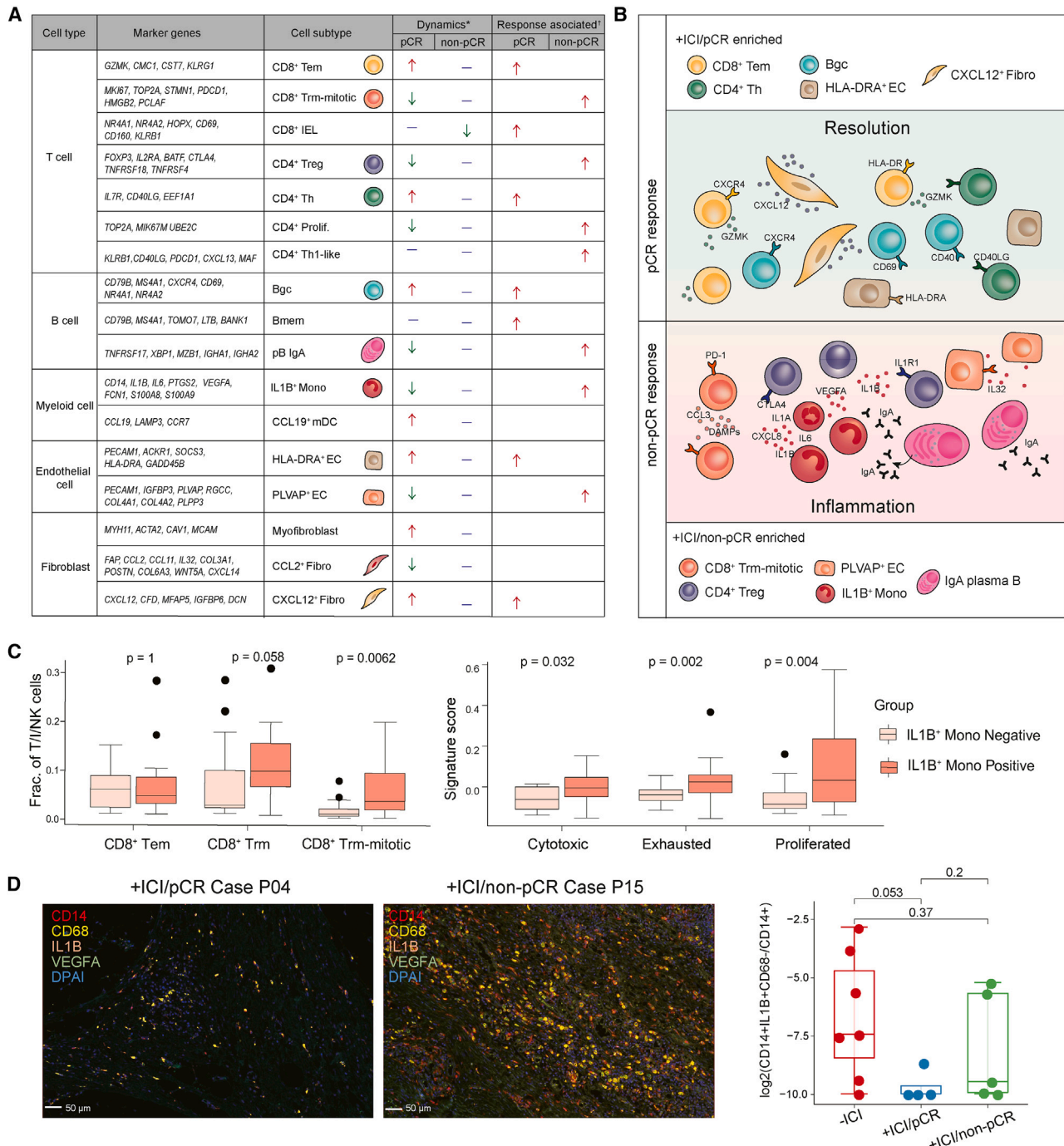


Figure 7. Proinflammatory IL1B⁺ Mono cells were enriched in non-pCR group

(A) Characteristics and summary of key immune and stromal cell cluster dynamics of ICI treatment. *Red (or green) arrows represent significant increase (or decrease) of cell clusters in +ICI/pCR and +ICI/non-pCR compared with -ICI, dashed lines represent no significant difference. †Red arrows represent significantly higher cell cluster frequency in either +ICI/pCR or +ICI/non-pCR.

(B) Difference of cell cluster between pCR and non-pCR and their association with inflammation.

(C) Quantification of cell cluster frequency representation among the IL1B⁺ Mono-positive and IL1B⁺ Mono-negative sample groups. The median and interquartile range are shown for each patient group. Two-sided Wilcoxon test.

(D) Representative images of mIHC staining indicating IL1B⁺CD14⁺CD68⁻ cells, in +ICI/pCR and +ICI/non-pCR samples. Each dot in boxplot presents the fractions of IL1B⁺CD14⁺CD68⁻ cells in each sample based on the IHC staining image. Two-sided Wilcoxon test.

Also see [Figure S7](#).

We reviewed the changes of all cell clusters in different treatment regimens and found that among all cell types, only CXCL12⁺ EC were significantly less in the celecoxib combination group than the anti-PD-1-only group, as shown in the supplementary figures (Figures S3B, S4A, S4I, S5B, S6B, and S6C). However, CXCL12⁺ EC was not pCR associated (Figure 6F). Consistent with this biological phenomenon, the results from the PICC study showed that although celecoxib combination regimen improved the pCR rate, the difference between PD-1 blockade monotherapy and celecoxib combination was not statistically significant (88% in the monotherapy group vs. 65% in the combination therapy group, $p = 0.23$).⁹ The possible explanation is that PD-1 blockade achieved a very high pCR rate in the neoadjuvant setting, which may obscure some contribution from celecoxib. Anyhow, our results provide clues about immune cell subsets that are most likely to be affected by celecoxib, which may be helpful for future study.

Limitations of our study include the small sample size and lack of pretreatment non-pCR samples. Further studies are needed to explore the mechanism of immune modulation by PD-1 blockade. In addition, due to the lack of pretreatment non-pCR samples, we were unable to identify cell clusters that are associated with pCR response in the baseline setting, which limited the significance of efficacy prediction. By comparing the differences between pCR and non-pCR after treatment, we identified potential targets to improve efficacy of ICI. However, how these results may apply to intrinsically resistant tumors (e.g., in stage IV disease) needs to be further explored. Since the actual tumor regression grade has reached more than 90% in non-pCR in this study, which is not completely the same as the concept of resistance in stage IV disease, which is defined as that the tumor volume does not shrink or even increase after treatment. It should be noted that the research aimed at improving pCR has important clinical significance, which is not only to prolong survival, but more importantly, to exempt surgery to protect organ function. The phenomenon found in sustaining non-pCR signature contributes to understanding the knowledge of complete response in neoadjuvant ICI treatment, and thus to identify patients who may be suitable for sphincter/organ-preserving or watch-and-wait strategies.

In conclusion, our study illuminates key immune and stromal cell subsets during ICI treatment and provides new insights into the cellular underpinnings of distinct responses to PD-1 blockade in patients with d-MMR/MSI-H CRC. Our study also provides evidence of an association between inflammation and ICI-induced treatment responses. These data also provide a rich resource for the identification of therapeutic targets for d-MMR/MSI-H CRC, which requires further investigation.

STAR★METHODS

Detailed methods are provided in the online version of this paper and include the following:

- KEY RESOURCES TABLE
- RESOURCE AVAILABILITY
 - Lead contact
 - Materials availability
 - Data and code availability

● EXPERIMENTAL MODEL AND SUBJECT DETAILS

- Patient population and clinical study
- *In vivo* mouse models

● METHOD DETAILS

- Sample collection and dissociation for scRNA-seq
- Single-cell RNA-seq library preparation and sequencing
- Multiplex fluorescence immunohistochemistry
- Luminex-based cytokine/chemokine detection for serum samples
- Tissue digestion and flow cytometry analysis for mouse samples
- Serum cytokine/chemokine data analysis
- Pre-processing of single cell RNA-seq data
- Unsupervised clustering analysis and identification of broad cell type
- Removing cells with high expression level of mitochondrial genes
- Dimensionality reduction using UMAP
- Re-clustering of broad cell types
- Identification of marker genes
- Differential expression and functional annotation
- Definition of gene signature score
- Gene set enrichment analysis
- Correlation analysis
- Cell-to-cell communication of scRNA-seq data
- Cell developmental trajectory
- Cell subtype abundance estimated from TCGA bulk gene expression profiles
- Correlative cell-cell interactions inferred by combined scRNA-seq and TCGA MSI-H CRC datasets

● QUANTIFICATION AND STATISTICAL ANALYSIS

SUPPLEMENTAL INFORMATION

Supplemental information can be found online at <https://doi.org/10.1016/j.ccell.2023.04.011>.

ACKNOWLEDGMENTS

This project was supported by National Natural Science Foundation of China, China (82272800, 81974369, 82102952), Science and Technology Program of Guangzhou, China (202206080011), National Natural Science Foundation of Guangdong Province, China (2021A1515010568), National Science Fund for Distinguished Young Scholars, China (82002944), and Key Technologies Research and Development Program of China, China (2019YFC1316003).

AUTHOR CONTRIBUTIONS

Conceptualization: Y.H.D., J.X.L., and H.B.H.; Methodology: J.X.L., C.Wu, H.B.H., G.Q., and Z.X.; Investigation: X.Q.W., F.B., and J.Q.Y.; Data Curation: Y.Z.L., J.X.L., C.Wu, and Z.H.J.; Resources: G.Q., Y.H., C.Wang, J.W.Z., Y.C., J.Y.L., Z.H.W., and Y.X.C.; Writing – Original Draft: Y.H.D., J.X.L., C.Wu., H.B.H., and Z.X.; Writing – Review & Editing: Y.H.D., J.X.L., and G.Q.; Funding Acquisition: Y.H.D., J.W.Z., and G.Q.; Supervision: Y.H.D.

DECLARATION OF INTERESTS

The authors declare no competing interests.

INCLUSION AND DIVERSITY

We support inclusive, diverse, and equitable conduct of research.

Received: July 8, 2022
Revised: January 6, 2023
Accepted: April 18, 2023
Published: May 11, 2023

REFERENCES

- Vilar, E., and Gruber, S.B. (2010). Microsatellite instability in colorectal cancer—the stable evidence. *Nat. Rev. Clin. Oncol.* *7*, 153–162. <https://doi.org/10.1038/nrclinonc.2009.237>.
- Giannakis, M., Mu, X.J., Shukla, S.A., Qian, Z.R., Cohen, O., Nishihara, R., Bahl, S., Cao, Y., Amin-Mansour, A., Yamauchi, M., et al. (2016). Genomic correlates of immune-cell infiltrates in colorectal carcinoma. *Cell Rep.* *15*, 857–865. <https://doi.org/10.1016/j.celrep.2016.03.075>.
- Llosa, N.J., Cruise, M., Tam, A., Wicks, E.C., Hechenbleikner, E.M., Taube, J.M., Blosser, R.L., Fan, H., Wang, H., Lubber, B.S., et al. (2015). The vigorous immune microenvironment of microsatellite instable colon cancer is balanced by multiple counter-inhibitory checkpoints. *Cancer Discov.* *5*, 43–51. <https://doi.org/10.1158/2159-8290.Cd-14-0863>.
- André, T., Shiu, K.K., Kim, T.W., Jensen, B.V., Jensen, L.H., Punt, C., Smith, D., Garcia-Carbonero, R., Benavides, M., Gibbs, P., et al. (2020). Pembrolizumab in microsatellite-Instability-high advanced colorectal cancer. *N. Engl. J. Med.* *383*, 2207–2218. <https://doi.org/10.1056/NEJMoa2017699>.
- Le, D.T., Kim, T.W., Van Cutsem, E., Geva, R., Jäger, D., Hara, H., Burge, M., O’Neil, B., Kavan, P., Yoshino, T., et al. (2020). Phase II open-label study of pembrolizumab in treatment-refractory, microsatellite instability-high/mismatch repair-deficient metastatic colorectal cancer: KEYNOTE-164. *J. Clin. Oncol.* *38*, 11–19. <https://doi.org/10.1200/jco.19.02107>.
- Le, D.T., Uram, J.N., Wang, H., Bartlett, B.R., Kemberling, H., Eyring, A.D., Skora, A.D., Lubber, B.S., Azad, N.S., Laheru, D., et al. (2015). PD-1 blockade in tumors with mismatch-repair deficiency. *N. Engl. J. Med.* *372*, 2509–2520. <https://doi.org/10.1056/NEJMoa1500596>.
- Overman, M.J., McDermott, R., Leach, J.L., Lonardi, S., Lenz, H.J., Morse, M.A., Desai, J., Hill, A., Axelson, M., Moss, R.A., et al. (2017). Nivolumab in patients with metastatic DNA mismatch repair-deficient or microsatellite instability-high colorectal cancer (CheckMate 142): an open-label, multicentre, phase 2 study. *Lancet Oncol.* *18*, 1182–1191. [https://doi.org/10.1016/s1470-2045\(17\)30422-9](https://doi.org/10.1016/s1470-2045(17)30422-9).
- Chalabi, M., Fanchi, L.F., Dijkstra, K.K., Van den Berg, J.G., Aalbers, A.G., Sikorska, K., Lopez-Yurda, M., Grootsholten, C., Beets, G.L., Snaebjornsson, P., et al. (2020). Neoadjuvant immunotherapy leads to pathological responses in MMR-proficient and MMR-deficient early-stage colon cancers. *Nat. Med.* *26*, 566–576. <https://doi.org/10.1038/s41591-020-0805-8>.
- Hu, H., Kang, L., Zhang, J., Wu, Z., Wang, H., Huang, M., Lan, P., Wu, X., Wang, C., Cao, W., et al. (2022). Neoadjuvant PD-1 blockade with toripalimab, with or without celecoxib, in mismatch repair-deficient or microsatellite instability-high, locally advanced, colorectal cancer (PICC): a single-centre, parallel-group, non-comparative, randomised, phase 2 trial. *Lancet Gastroenterol. Hepatol.* *7*, 38–48. [https://doi.org/10.1016/s2468-1253\(21\)00348-4](https://doi.org/10.1016/s2468-1253(21)00348-4).
- Cercek, A., Lumish, M., Sinopoli, J., Weiss, J., Shia, J., Lamendola-Essel, M., El Dika, I.H., Segal, N., Shcherba, M., Sugarman, R., et al. (2022). PD-1 blockade in mismatch repair-deficient, locally advanced rectal cancer. *N. Engl. J. Med.* *386*, 2363–2376. <https://doi.org/10.1056/NEJMoa2201445>.
- Bortolomeazzi, M., Keddar, M.R., Montorsi, L., Acha-Sagredo, A., Benedetti, L., Temelkovski, D., Choi, S., Petrov, N., Todd, K., Wai, P., et al. (2021). Immunogenomics of colorectal cancer response to checkpoint blockade: analysis of the KEYNOTE 177 trial and validation cohorts. *Gastroenterology* *161*, 1179–1193. <https://doi.org/10.1053/j.gastro.2021.06.064>.
- Bassez, A., Vos, H., Van Dyck, L., Floris, G., Arijis, I., Desmedt, C., Boeckx, B., Vanden Bempt, M., Nevelsteen, I., Lambein, K., et al. (2021). A single-cell map of intratumoral changes during anti-PD1 treatment of patients with breast cancer. *Nat. Med.* *27*, 820–832. <https://doi.org/10.1038/s41591-021-01323-8>.
- Bi, K., He, M.X., Bakouny, Z., Kanodia, A., Napolitano, S., Wu, J., Grimaldi, G., Braun, D.A., Cuoco, M.S., Mayorga, A., et al. (2021). Tumor and immune reprogramming during immunotherapy in advanced renal cell carcinoma. *Cancer Cell* *39*, 649–661.e5. <https://doi.org/10.1016/j.ccell.2021.02.015>.
- Jerby-Arnon, L., Shah, P., Cuoco, M.S., Rodman, C., Su, M.J., Melms, J.C., Leeson, R., Kanodia, A., Mei, S., Lin, J.R., et al. (2018). A cancer cell program promotes T cell exclusion and resistance to checkpoint blockade. *Cell* *175*, 984–997.e24. <https://doi.org/10.1016/j.cell.2018.09.006>.
- Zhang, Y., Chen, H., Mo, H., Hu, X., Gao, R., Zhao, Y., Liu, B., Niu, L., Sun, X., Yu, X., et al. (2021). Single-cell analyses reveal key immune cell subsets associated with response to PD-L1 blockade in triple-negative breast cancer. *Cancer Cell* *39*, 1578–1593.e8. <https://doi.org/10.1016/j.ccell.2021.09.010>.
- Li, H., van der Leun, A.M., Yofe, I., Lubling, Y., Gelbard-Solodkin, D., van Akkooi, A.C.J., van den Braber, M., Rozeman, E.A., Haanen, J.B., Blank, C.U., et al. (2019). Dysfunctional CD8 T cells form a proliferative, dynamically regulated compartment within human melanoma. *Cell* *176*, 775–789.e18. <https://doi.org/10.1016/j.cell.2018.11.043>.
- Zheng, Y., Chen, Z., Han, Y., Han, L., Zou, X., Zhou, B., Hu, R., Hao, J., Bai, S., Xiao, H., et al. (2020). Immune suppressive landscape in the human esophageal squamous cell carcinoma microenvironment. *Nat. Commun.* *11*, 6268. <https://doi.org/10.1038/s41467-020-20019-0>.
- Milner, J.J., Toma, C., Yu, B., Zhang, K., Omilusik, K., Phan, A.T., Wang, D., Getzler, A.J., Nguyen, T., Crotty, S., et al. (2017). Runx3 programs CD8(+) T cell residency in non-lymphoid tissues and tumours. *Nature* *552*, 253–257. <https://doi.org/10.1038/nature24993>.
- Savas, P., Virassamy, B., Ye, C., Salim, A., Mintoff, C.P., Caramia, F., Salgado, R., Byrne, D.J., Teo, Z.L., Dushyanthen, S., et al. (2018). Single-cell profiling of breast cancer T cells reveals a tissue-resident memory subset associated with improved prognosis. *Nat. Med.* *24*, 986–993. <https://doi.org/10.1038/s41591-018-0078-7>.
- Duhen, T., Duhen, R., Montler, R., Moses, J., Moudgil, T., de Miranda, N.F., Goodall, C.P., Blair, T.C., Fox, B.A., McDermott, J.E., et al. (2018). Co-expression of CD39 and CD103 identifies tumor-reactive CD8 T cells in human solid tumors. *Nat. Commun.* *9*, 2724. <https://doi.org/10.1038/s41467-018-05072-0>.
- Clarke, J., Panwar, B., Madrigal, A., Singh, D., Gujar, R., Wood, O., Chee, S.J., Eschweiler, S., King, E.V., Awad, A.S., et al. (2019). Single-cell transcriptomic analysis of tissue-resident memory T cells in human lung cancer. *J. Exp. Med.* *216*, 2128–2149. <https://doi.org/10.1084/jem.20190249>.
- Prasad, S., Hu, S., Sheng, W.S., Chauhan, P., Singh, A., and Lokensgard, J.R. (2017). The PD-1: PD-L1 pathway promotes development of brain-resident memory T cells following acute viral encephalitis. *J. Neuroinflammation* *14*, 82. <https://doi.org/10.1186/s12974-017-0860-3>.
- Liu, B., Hu, X., Feng, K., Gao, R., Xue, Z., Zhang, S., Zhang, Y., Corse, E., Hu, Y., Han, W., and Zhang, Z. (2022). Temporal single-cell tracing reveals clonal revival and expansion of precursor exhausted T cells during anti-PD-1 therapy in lung cancer. *Nat. Cancer* *3*, 108–121. <https://doi.org/10.1038/s43018-021-00292-8>.
- Wei, S.C., Levine, J.H., Cogdill, A.P., Zhao, Y., Anang, N.A.S., Andrews, M.C., Sharma, P., Wang, J., Wargo, J.A., Pe’er, D., and Allison, J.P. (2017). Distinct cellular mechanisms underlie anti-CTLA-4 and anti-PD-1 checkpoint blockade. *Cell* *170*, 1120–1133.e17. <https://doi.org/10.1016/j.cell.2017.07.024>.
- Yost, K.E., Satpathy, A.T., Wells, D.K., Qi, Y., Wang, C., Kageyama, R., McNamara, K.L., Granja, J.M., Sarin, K.Y., Brown, R.A., et al. (2019). Clonal replacement of tumor-specific T cells following PD-1 blockade. *Nat. Med.* *25*, 1251–1259. <https://doi.org/10.1038/s41591-019-0522-3>.
- Sade-Feldman, M., Yizhak, K., Bjorgaard, S.L., Ray, J.P., de Boer, C.G., Jenkins, R.W., Lieb, D.J., Chen, J.H., Frederick, D.T., Barzily-Rokni, M.,

- et al. (2018). Defining T cell states associated with response to checkpoint immunotherapy in melanoma. *Cell* 175, 998–1013.e20. <https://doi.org/10.1016/j.cell.2018.10.038>.
27. Miller, B.C., Sen, D.R., Al Abohy, R., Bi, K., Virkud, Y.V., LaFleur, M.W., Yates, K.B., Lako, A., Felt, K., Naik, G.S., et al. (2019). Subsets of exhausted CD8(+) T cells differentially mediate tumor control and respond to checkpoint blockade. *Nat. Immunol.* 20, 326–336. <https://doi.org/10.1038/s41590-019-0312-6>.
28. Siddiqui, I., Schaeuble, K., Chennupati, V., Fuertes Marraco, S.A., Calderon-Copete, S., Pais Ferreira, D., Carmona, S.J., Scarpellino, L., Gfeller, D., Pradervand, S., et al. (2019). Intratumoral Tcf1(+)PD-1(+) CD8(+) T cells with stem-like properties promote tumor control in response to vaccination and checkpoint blockade immunotherapy. *Immunity* 50, 195–211.e10. <https://doi.org/10.1016/j.immuni.2018.12.021>.
29. Gubin, M.M., Esaulova, E., Ward, J.P., Malkova, O.N., Runci, D., Wong, P., Noguchi, T., Arthur, C.D., Meng, W., Alspach, E., et al. (2018). High-dimensional analysis delineates myeloid and lymphoid compartment remodeling during successful immune-checkpoint cancer therapy. *Cell* 175, 1014–1030.e19. <https://doi.org/10.1016/j.cell.2018.09.030>.
30. Tanaka, A., and Sakaguchi, S. (2017). Regulatory T cells in cancer immunotherapy. *Cell Res.* 27, 109–118. <https://doi.org/10.1038/cr.2016.151>.
31. Borst, J., Ahrends, T., Bąbala, N., Melief, C.J.M., and Kastenmüller, W. (2018). CD4(+) T cell help in cancer immunology and immunotherapy. *Nat. Rev. Immunol.* 18, 635–647. <https://doi.org/10.1038/s41577-018-0044-0>.
32. Byrne, K.T., and Vonderheide, R.H. (2016). CD40 stimulation obviates innate sensors and drives T cell immunity in cancer. *Cell Rep.* 15, 2719–2732. <https://doi.org/10.1016/j.celrep.2016.05.058>.
33. Elgueta, R., Benson, M.J., de Vries, V.C., Wasiuk, A., Guo, Y., and Noelle, R.J. (2009). Molecular mechanism and function of CD40/CD40L engagement in the immune system. *Immunol. Rev.* 229, 152–172. <https://doi.org/10.1111/j.1600-065X.2009.00782.x>.
34. Brooks, J.F., Tan, C., Mueller, J.L., Hibiya, K., Hiwa, R., Vykunta, V., and Zikherman, J. (2021). Negative feedback by NUR77/Nr4a1 restrains B cell clonal dominance during early T-dependent immune responses. *Cell Rep.* 36, 109645. <https://doi.org/10.1016/j.celrep.2021.109645>.
35. Cabrita, R., Lauss, M., Sanna, A., Donia, M., Skaarup Larsen, M., Mitra, S., Johansson, I., Phung, B., Harbst, K., Vallon-Christersson, J., et al. (2020). Tertiary lymphoid structures improve immunotherapy and survival in melanoma. *Nature* 577, 561–565. <https://doi.org/10.1038/s41586-019-1914-8>.
36. Meednu, N., Rangel-Moreno, J., Zhang, F., Escalera-Rivera, K., Corsiero, E., Prediletto, E., DiCarlo, E., Goodman, S., Donlin, L.T., Raychauduri, S., et al. (2022). Dynamic spectrum of ectopic lymphoid B cell activation and hypermutation in the RA synovium characterized by NR4A nuclear receptor expression. *Cell Rep.* 39, 110766. <https://doi.org/10.1016/j.celrep.2022.110766>.
37. van Hooren, L., Vaccaro, A., Ramachandran, M., Vazaios, K., Libard, S., van de Walle, T., Georganaki, M., Huang, H., Pietilä, I., Lau, J., et al. (2021). Agonistic CD40 therapy induces tertiary lymphoid structures but impairs responses to checkpoint blockade in glioma. *Nat. Commun.* 12, 4127. <https://doi.org/10.1038/s41467-021-24347-7>.
38. Zhang, L., Li, Z., Skrzypczynska, K.M., Fang, Q., Zhang, W., O'Brien, S.A., He, Y., Wang, L., Zhang, Q., Kim, A., et al. (2020). Single-cell analyses inform mechanisms of myeloid-targeted Therapies in colon cancer. *Cell* 181, 442–459.e29. <https://doi.org/10.1016/j.cell.2020.03.048>.
39. Zhao, H., Wu, L., Yan, G., Chen, Y., Zhou, M., Wu, Y., and Li, Y. (2021). Inflammation and tumor progression: signaling pathways and targeted intervention. *Signal Transduct. Target. Ther.* 6, 263. <https://doi.org/10.1038/s41392-021-00658-5>.
40. Pelka, K., Hofree, M., Chen, J.H., Sarkizova, S., Pirl, J.D., Jorgji, V., Bejnood, A., Dionne, D., Ge, W.H., Xu, K.H., et al. (2021). Spatially organized multicellular immune hubs in human colorectal cancer. *Cell* 184, 4734–4752.e20. <https://doi.org/10.1016/j.cell.2021.08.003>.
41. Asrir, A., Tardiveau, C., Coudert, J., Laffont, R., Blanchard, L., Bellard, E., Veerman, K., Bettini, S., Lafouresse, F., Vina, E., et al. (2022). Tumor-associated high endothelial venules mediate lymphocyte entry into tumors and predict response to PD-1 plus CTLA-4 combination immunotherapy. *Cancer Cell* 40, 318–334.e9. <https://doi.org/10.1016/j.ccell.2022.01.002>.
42. Bagaev, A., Kotlov, N., Nomie, K., Svekolkin, V., Gafurov, A., Isaeva, O., Osokin, N., Kozlov, I., Frenkel, F., Gancharova, O., et al. (2021). Conserved pan-cancer microenvironment subtypes predict response to immunotherapy. *Cancer Cell* 39, 845–865.e7. <https://doi.org/10.1016/j.ccell.2021.04.014>.
43. Mariathasan, S., Turley, S.J., Nickles, D., Castiglioni, A., Yuen, K., Wang, Y., Kadel, E.E., III, Koeppen, H., Astarita, J.L., Cubas, R., et al. (2018). TGFβ attenuates tumour response to PD-L1 blockade by contributing to exclusion of T cells. *Nature* 554, 544–548. <https://doi.org/10.1038/nature25501>.
44. Kinchen, J., Chen, H.H., Parikh, K., Antanaviciute, A., Jagielowicz, M., Fawcner-Corbett, D., Ashley, N., Cubitt, L., Mellado-Gomez, E., Attar, M., et al. (2018). Structural remodeling of the human colonic mesenchyme in inflammatory bowel disease. *Cell* 175, 372–386.e17. <https://doi.org/10.1016/j.cell.2018.08.067>.
45. Feig, C., Jones, J.O., Kraman, M., Wells, R.J.B., Deonarine, A., Chan, D.S., Connell, C.M., Roberts, E.W., Zhao, Q., Caballero, O.L., et al. (2013). Targeting CXCL12 from FAP-expressing carcinoma-associated fibroblasts synergizes with anti-PD-L1 immunotherapy in pancreatic cancer. *Proc. Natl. Acad. Sci. USA* 110, 20212–20217. <https://doi.org/10.1073/pnas.1320318110>.
46. Krishnamurthy, A.T., and Turley, S.J. (2020). Lymph node stromal cells: cartographers of the immune system. *Nat. Immunol.* 21, 369–380. <https://doi.org/10.1038/s41590-020-0635-3>.
47. Rodda, L.B., Bannard, O., Ludewig, B., Nagasawa, T., and Cyster, J.G. (2015). Phenotypic and morphological properties of germinal center dark zone Cxcl12-expressing reticular cells. *J. Immunol.* 195, 4781–4791. <https://doi.org/10.4049/jimmunol.1501191>.
48. Vestweber, D. (2015). How leukocytes cross the vascular endothelium. *Nat. Rev. Immunol.* 15, 692–704. <https://doi.org/10.1038/nri3908>.
49. Carman, C.V., and Martinelli, R. (2015). T lymphocyte-endothelial interactions: emerging understanding of Trafficking and antigen-specific immunity. *Front. Immunol.* 6, 603. <https://doi.org/10.3389/fimmu.2015.00603>.
50. Savage, C.O., Brooks, C.J., Harcourt, G.C., Picard, J.K., King, W., Sansom, D.M., and Willcox, N. (1995). Human vascular endothelial cells process and present autoantigen to human T cell lines. *Int. Immunol.* 7, 471–479. <https://doi.org/10.1093/intimm/7.3.471>.
51. Ma, W., and Pober, J.S. (1998). Human endothelial cells effectively costimulate cytokine production by, but not differentiation of, naive CD4+ T cells. *J. Immunol.* 161, 2158–2167.
52. Puram, S.V., Tirosh, I., Parikh, A.S., Patel, A.P., Yizhak, K., Gillespie, S., Rodman, C., Luo, C.L., Mroz, E.A., Emerick, K.S., et al. (2017). Single-cell transcriptomic analysis of primary and metastatic tumor ecosystems in head and neck cancer. *Cell* 171, 1611–1624.e24. <https://doi.org/10.1016/j.cell.2017.10.044>.
53. Tirosh, I., Izar, B., Prakadan, S.M., Wadsworth, M.H., 2nd, Treacy, D., Trombetta, J.J., Rotem, A., Rodman, C., Lian, C., Murphy, G., et al. (2016). Dissecting the multicellular ecosystem of metastatic melanoma by single-cell RNA-seq. *Science* 352, 189–196. <https://doi.org/10.1126/science.aad0501>.
54. Hong, J.T., Son, D.J., Lee, C.K., Yoon, D.Y., Lee, D.H., and Park, M.H. (2017). Interleukin 32, inflammation and cancer. *Pharmacol. Ther.* 174, 127–137. <https://doi.org/10.1016/j.pharmthera.2017.02.025>.
55. Erez, N., Truitt, M., Olson, P., Arron, S.T., and Hanahan, D. (2010). Cancer-associated fibroblasts are activated in incipient neoplasia to orchestrate tumor-promoting inflammation in an NF-κappaB-Dependent manner. *Cancer Cell* 17, 135–147. <https://doi.org/10.1016/j.ccr.2009.12.041>.
56. Ma, Z., Li, X., Mao, Y., Wei, C., Huang, Z., Li, G., Yin, J., Liang, X., and Liu, Z. (2022). Interferon-dependent SLC14A1(+) cancer-associated

- fibroblasts promote cancer stemness via WNT5A in bladder cancer. *Cancer Cell* 40, 1550–1565.e1557. <https://doi.org/10.1016/j.ccell.2022.11.005>.
57. Sharma, A., Seow, J.J.W., Dutertre, C.A., Pai, R., Blériot, C., Mishra, A., Wong, R.M.M., Singh, G.S.N., Sudhagar, S., Khalilnezhad, S., et al. (2020). Onco-fetal reprogramming of endothelial cells drives immunosuppressive macrophages in hepatocellular carcinoma. *Cell* 183, 377–394.e21. <https://doi.org/10.1016/j.cell.2020.08.040>.
58. Headland, S.E., and Norling, L.V. (2015). The resolution of inflammation: principles and challenges. *Semin. Immunol.* 27, 149–160. <https://doi.org/10.1016/j.smim.2015.03.014>.
59. Mantovani, A., Barajon, I., and Garlanda, C. (2018). IL-1 and IL-1 regulatory pathways in cancer progression and therapy. *Immunol. Rev.* 281, 57–61. <https://doi.org/10.1111/immr.12614>.
60. Zhang, Q., Zhu, B., and Li, Y. (2017). Resolution of cancer-promoting inflammation: a new approach for anticancer therapy. *Front. Immunol.* 8, 71. <https://doi.org/10.3389/fimmu.2017.00071>.
61. Schenkel, J.M., Fraser, K.A., Vezys, V., and Masopust, D. (2013). Sensing and alarm function of resident memory CD8⁺ T cells. *Nat. Immunol.* 14, 509–513. <https://doi.org/10.1038/ni.2568>.
62. Schenkel, J.M., Fraser, K.A., Beura, L.K., Pauken, K.E., Vezys, V., and Masopust, D. (2014). T cell memory. Resident memory CD8 T cells trigger protective innate and adaptive immune responses. *Science* 346, 98–101. <https://doi.org/10.1126/science.1254536>.
63. Mackay, L.K., Stock, A.T., Ma, J.Z., Jones, C.M., Kent, S.J., Mueller, S.N., Heath, W.R., Carbone, F.R., and Gebhardt, T. (2012). Long-lived epithelial immunity by tissue-resident memory T (TRM) cells in the absence of persisting local antigen presentation. *Proc. Natl. Acad. Sci. USA* 109, 7037–7042. <https://doi.org/10.1073/pnas.1202288109>.
64. Mijnheer, G., Lutter, L., Mokry, M., van der Wal, M., Scholman, R., Fleskens, V., Pandit, A., Tao, W., Wekking, M., Vervoort, S., et al. (2021). Conserved human effector Treg cell transcriptomic and epigenetic signature in arthritic joint inflammation. *Nat. Commun.* 12, 2710. <https://doi.org/10.1038/s41467-021-22975-7>.
65. Shalpour, S., Lin, X.J., Bastian, I.N., Brain, J., Burt, A.D., Aksenov, A.A., Vrbnac, A.F., Li, W., Perkins, A., Matsutani, T., et al. (2017). Inflammation-induced IgA⁺ cells dismantle anti-liver cancer immunity. *Nature* 551, 340–345. <https://doi.org/10.1038/nature24302>.
66. de Visser, K.E., Korets, L.V., and Coussens, L.M. (2005). De novo carcinogenesis promoted by chronic inflammation is B lymphocyte dependent. *Cancer Cell* 7, 411–423. <https://doi.org/10.1016/j.ccr.2005.04.014>.
67. Roumenina, L.T., Daugan, M.V., Noé, R., Petitprez, F., Vano, Y.A., Sanchez-Salas, R., Becht, E., Meilleroux, J., Clec'h, B.L., Giraldo, N.A., et al. (2019). Tumor cells hijack macrophage-produced complement C1q to promote tumor growth. *Cancer Immunol. Res.* 7, 1091–1105. <https://doi.org/10.1158/2326-6066.Cir-18-0891>.
68. Pilette, C., Detry, B., Guisset, A., Gabriels, J., and Sibille, Y. (2010). Induction of interleukin-10 expression through Fc α receptor in human monocytes and monocyte-derived dendritic cells: role of p38 MAPK kinase. *Immunol. Cell Biol.* 88, 486–493. <https://doi.org/10.1038/icb.2009.120>.
69. de Jonge, K., Tillé, L., Lourenco, J., Maby-El Hajjami, H., Nassiri, S., Racle, J., Gfeller, D., Delorenzi, M., Verdel, G., Baumgaertner, P., and Speiser, D.E. (2021). Inflammatory B cells correlate with failure to checkpoint blockade in melanoma patients. *Oncolimmunology* 10, 1873585. <https://doi.org/10.1080/2162402x.2021.1873585>.
70. Guo, X., Zhang, Y., Zheng, L., Zheng, C., Song, J., Zhang, Q., Kang, B., Liu, Z., Jin, L., Xing, R., et al. (2018). Global characterization of T cells in non-small-cell lung cancer by single-cell sequencing. *Nat. Med.* 24, 978–985. <https://doi.org/10.1038/s41591-018-0045-3>.
71. Thommen, D.S., Koelzer, V.H., Herzig, P., Roller, A., Trefny, M., Dimeloe, S., Kiialainen, A., Hanhart, J., Schill, C., Hess, C., et al. (2018). A transcriptionally and functionally distinct PD-1(+) CD8(+) T cell pool with predictive potential in non-small-cell lung cancer treated with PD-1 blockade. *Nat. Med.* 24, 994–1004. <https://doi.org/10.1038/s41591-018-0057-z>.
72. Zhang, L., Yu, X., Zheng, L., Zhang, Y., Li, Y., Fang, Q., Gao, R., Kang, B., Zhang, Q., Huang, J.Y., et al. (2018). Lineage tracking reveals dynamic relationships of T cells in colorectal cancer. *Nature* 564, 268–272. <https://doi.org/10.1038/s41586-018-0694-x>.
73. Luoma, A.M., Suo, S., Williams, H.L., Sharova, T., Sullivan, K., Manos, M., Bowling, P., Hodi, F.S., Rahma, O., Sullivan, R.J., et al. (2020). Molecular pathways of colon inflammation induced by cancer immunotherapy. *Cell* 182, 655–671.e22. <https://doi.org/10.1016/j.cell.2020.06.001>.
74. Lavin, Y., Kobayashi, S., Leader, A., Amir, E.A.D., Elefant, N., Bigenwald, C., Remark, R., Sweeney, R., Becker, C.D., Levine, J.H., et al. (2017). Innate immune landscape in early lung adenocarcinoma by paired single-cell analyses. *Cell* 169, 750–765.e17. <https://doi.org/10.1016/j.cell.2017.04.014>.
75. Davidson, S., Efremova, M., Riedel, A., Mahata, B., Pramanik, J., Huuhtanen, J., Kar, G., Vento-Tormo, R., Hagai, T., Chen, X., et al. (2020). Single-cell RNA sequencing reveals a dynamic stromal niche that supports tumor growth. *Cell Rep.* 31, 107628. <https://doi.org/10.1016/j.celrep.2020.107628>.
76. Combes, A.J., Samad, B., Tsui, J., Chew, N.W., Yan, P., Reeder, G.C., Kushnood, D., Shen, A., Davidson, B., Barczak, A.J., et al. (2022). Discovering dominant tumor immune archetypes in a pan-cancer census. *Cell* 185, 184–203.e19. <https://doi.org/10.1016/j.cell.2021.12.004>.
77. Thorsson, V., Gibbs, D.L., Brown, S.D., Wolf, D., Bortone, D.S., Ou Yang, T.H., Porta-Pardo, E., Gao, G.F., Plaisier, C.L., Eddy, J.A., et al. (2018). The immune landscape of cancer. *Immunity* 48, 812–830.e14. <https://doi.org/10.1016/j.immuni.2018.03.023>.
78. Kieffer, Y., Hocine, H.R., Gentric, G., Pelon, F., Bernard, C., Bourachot, B., Lameiras, S., Albergante, L., Bonneau, C., Guyard, A., et al. (2020). Single-cell analysis reveals fibroblast clusters linked to immunotherapy resistance in cancer. *Cancer Discov.* 10, 1330–1351. <https://doi.org/10.1158/2159-8290.Cd-19-1384>.
79. Dominguez, C.X., Müller, S., Keerthivasan, S., Koeppen, H., Hung, J., Gierke, S., Breart, B., Foreman, O., Bainbridge, T.W., Castiglioni, A., et al. (2020). Single-cell RNA sequencing reveals stromal evolution into LRRC15(+) myofibroblasts as a determinant of patient response to cancer immunotherapy. *Cancer Discov.* 10, 232–253. <https://doi.org/10.1158/2159-8290.Cd-19-0644>.
80. Hao, Y., Hao, S., Andersen-Nissen, E., Mauck, W.M., 3rd, Zheng, S., Butler, A., Lee, M.J., Wilk, A.J., Darby, C., Zager, M., et al. (2021). Integrated analysis of multimodal single-cell data. *Cell* 184, 3573–3587.e29. <https://doi.org/10.1016/j.cell.2021.04.048>.
81. Korotkevich, G., Sukhov, V., Budin, N., Shpak, B., Artyomov, M.N., and Sergushichev, A. (2019). Fast gene set enrichment analysis. Preprint at bioRxiv. <https://doi.org/10.1101/060012>.
82. Jin, S., Guerrero-Juarez, C.F., Zhang, L., Chang, I., Ramos, R., Kuan, C.H., Myung, P., Plikus, M.V., and Nie, Q. (2021). Inference and analysis of cell-cell communication using CellChat. *Nat. Commun.* 12, 1088. <https://doi.org/10.1038/s41467-021-21246-9>.
83. Qiu, X., Mao, Q., Tang, Y., Wang, L., Chawla, R., Pliner, H.A., and Trapnell, C. (2017). Reversed graph embedding resolves complex single-cell trajectories. *Nat. Methods* 14, 979–982. <https://doi.org/10.1038/nmeth.4402>.
84. Fawcner-Corbett, D., Antanaviciute, A., Parikh, K., Jagielowicz, M., Gerós, A.S., Gupta, T., Ashley, N., Khamis, D., Fowler, D., Morrissey, E., et al. (2021). Spatiotemporal analysis of human intestinal development at single-cell resolution. *Cell* 184, 810–826.e23. <https://doi.org/10.1016/j.cell.2020.12.016>.
85. Pijuan-Sala, B., Griffiths, J.A., Guibentif, C., Hiscock, T.W., Jawaid, W., Calero-Nieto, F.J., Mulas, C., Ibarra-Soria, X., Tyser, R.C.V., Ho, D.L.L., et al. (2019). A single-cell molecular map of mouse gastrulation and early organogenesis. *Nature* 566, 490–495. <https://doi.org/10.1038/s41586-019-0933-9>.
86. Squair, J.W., Gautier, M., Kathe, C., Anderson, M.A., James, N.D., Hutson, T.H., Hudelle, R., Qaiser, T., Matson, K.J.E., Barraud, Q., et al. (2021). Confronting false discoveries in single-cell differential expression. *Nat. Commun.* 12, 5692. <https://doi.org/10.1038/s41467-021-25960-2>.

87. Wu, T., Hu, E., Xu, S., Chen, M., Guo, P., Dai, Z., Feng, T., Zhou, L., Tang, W., Zhan, L., et al. (2021). clusterProfiler 4.0: a universal enrichment tool for interpreting omics data. *Innovation* 2, 100141. <https://doi.org/10.1016/j.xinn.2021.100141>.
88. Whitfield, M.L., George, L.K., Grant, G.D., and Perou, C.M. (2006). Common markers of proliferation. *Nat. Rev. Cancer* 6, 99–106. <https://doi.org/10.1038/nrc1802>.
89. Liberzon, A., Birger, C., Thorvaldsdóttir, H., Ghandi, M., Mesirov, J.P., and Tamayo, P. (2015). The Molecular Signatures Database (MSigDB) hallmark gene set collection. *Cell Syst.* 1, 417–425. <https://doi.org/10.1016/j.cels.2015.12.004>.
90. Bonneville, R., Krook, M.A., Kautto, E.A., Miya, J., Wing, M.R., Chen, H.Z., Reeser, J.W., Yu, L., and Roychowdhury, S. (2017). Landscape of microsatellite instability across 39 cancer types. *JCO Precis. Oncol.* 2017, 1–15. <https://doi.org/10.1200/po.17.00073>.

STAR★METHODS

KEY RESOURCES TABLE

REAGENT or RESOURCE	SOURCE	IDENTIFIER
Antibodies		
Rabbit anti-human CD4	Abcam	Cat# ab133616; RRID: AB_2750883
Mouse anti-human FOXP3	Abcam	Cat# ab20034; RRID: AB_445284
Rabbit anti-human CTLA4	Abcam	Cat# ab237712; RRID: AB_2905652
Rabbit anti-human TIM3	Abcam	Cat# ab241332; RRID: AB_2888936
Rabbit anti-human CD68	Abcam	Cat# ab213363; RRID: AB_2801637
Rabbit anti-human IL1B	Novus	Cat# NB600-633; RRID: AB_10001060
Rabbit anti-human CD14	Abcam	Cat# ab133335; RRID: AB_2889158
Mouse anti-human VEGFA (VG-1)	Abcam	Cat# ab1316; RRID: AB_299738
Mouse anti-human KI-67	CST	Cat# 9449; RRID: AB_2797703
Rabbit anti-human HLA-DR	Abcam	Cat# ab92511; RRID: AB_10563656
Rabbit anti-human CD3	Dako	Cat# A0452; RRID: AB_2335677
Rabbit anti-human CD8	Abcam	Cat# ab178089; RRID: AB_2756374
Mouse anti-human CD20	Proteintech	Cat# 60271-1-Ig; RRID: AB_2881391
Rabbit anti-human CD40	Abcam	Cat# ab224639; RRID: AB_2883981
anti-mouse CD8	BioLegend	Cat# 100712; RRID: AB_312751
anti-mouse CD45-FITC	BioLegend	Cat# 103108; RRID: AB_312973
anti-mouse CD45-PE/Cyanine7	BioLegend	Cat# 103114; RRID: AB_312979
anti-mouse CD279 (PD-1)	BioLegend	Cat# 135218; RRID: AB_2561447
anti-mouse CD4	BioLegend	Cat# 100412; RRID: AB_312697
anti-mouse CD40	BioLegend	Cat# 124612; RRID: AB_1134072
anti-mouse CD19	BioLegend	Cat# 115549; RRID: AB_2563066
anti-mouse FOXP3	BioLegend	Cat# 126406; RRID: AB_1089113
anti-mouse CD25	BioLegend	Cat# 102008; RRID: AB_312857
anti-human CD8	Zsbio	Cat# ZA-0508; RRID: AB_2890107
anti-human CD68	Zsbio	Cat# ZM-0060; RRID: AB_2904190
anti-human CD163	Zsbio	Cat# ZM-0428; RRID: NA
anti-human CD57	Zsbio	Cat# ZM-0058; RRID: NA
anti-human PD-1	Zsbio	Cat# ZM-0381; RRID: AB_2921363
anti-human PD-L1	CST	Cat# 13684; RRID: AB_2687655
Biological samples		
Human primary CRC samples	The sixth affiliated hospital of Sun Yat-sen University	#IRB 2021ZSLYEC-173, See Table S1 for details
Human adjacent normal tissues from CRC patients	The sixth affiliated hospital of Sun Yat-sen University	#IRB 2021ZSLYEC-173, See Table S1 for details
Human peripheral blood from CRC patients	The sixth affiliated hospital of Sun Yat-sen University	#IRB 2021ZSLYEC-173
Paraffin-embedded formalin fixed slides prepared from colon biopsy and surgical samples	The sixth affiliated hospital of Sun Yat-sen University	#IRB 2021ZSLYEC-173

(Continued on next page)

Continued

REAGENT or RESOURCE	SOURCE	IDENTIFIER
Critical commercial assays		
Human XL Cytokine Luminex Performance Panel Premixed Kit	Luminex	Cat# LKTM014
Sequencing: Chromium Single Cell 3' Library & Gel Bead Kit v2	10X Genomics	Cat# PN-120237
Sequencing: Chromium Single Cell 3' Library & Gel Bead Kit v3	10X Genomics	Cat# PN-1000075
Deposited data		
Processed single cell RNA-seq data in human dMMR/MSI-H CRC patients	This paper	GEO: GSE205506
TCGA COAD and READ datasets	GDC data portal	https://portal.gdc.cancer.gov/
Experimental models: Cell lines		
MC38	BMCR/NICR	Cat# 1101MOU-PUMC000523
Experimental models: Organisms/strains		
C57/BL6N mice	Jiangsu GemPharmatech	C57BL/6NGrl
Software and algorithms		
Cell Ranger-4.1.0	10 X Genomics	http://10xgenomics.com/
R-4.1.0	The R Foundation	https://www.r-project.org/
Seurat-4.1.0	Hao et al. ⁸⁰	https://satijalab.org/seurat/
fgsea (v1.18.0, R package)	Korotkevich et al. ⁸¹	https://bioconductor.org/packages/release/bioc/html/fgsea.html
CellChat (version 1.1.3)	Jin et al. ⁸²	https://github.com/sqjin/CellChat
Monocle2 (v2.10.1)	Qiu et al. ⁸³	https://github.com/cole-trapnellab/monocle-release

RESOURCE AVAILABILITY

Lead contact

Further information and requests for resources and reagents should be directed to and will be fulfilled by the Lead Contact, Yanhong Deng (dengyanh@mail.sysu.edu.cn).

Materials availability

This study did not generate new unique reagents.

Data and code availability

Processed single cell RNA-seq data of this study can be obtain from Gene Expression Omnibus (GEO) with an accession number of GSE205506. The raw FASTQ files in this study will be provided for scientific research upon request complying with the law due to human patient privacy concerns. Code used for all processing and analysis is available upon request.

EXPERIMENTAL MODEL AND SUBJECT DETAILS

Patient population and clinical study

Patient cohorts were from a randomized phase 2 PICC study (NCT03926338), with locally advanced, primary invasive carcinoma of the d-MMR/MSI-H colon and rectum treated with toripalimab with or without celecoxib for six cycles before curative surgical resection.⁹ The primary goal of the study was to investigated the efficacy and safety of PD-1 blockade with toripalimab, with or without the COX-2 inhibitor celecoxib, as neoadjuvant treatment for d-MMR/MSI-H locally advanced CRCs. The study enrolled 34 patients between May 1, 2019, and April 1, 2021. In both treatment groups, toripalimab 3 mg/kg (Junshi BioSciences, Shanghai, China) was given intravenously over 30 min on day 1 of each 14-day cycle, for six cycles, before surgical resection. Patients in the toripalimab plus celecoxib group were also given celecoxib 200 mg (Pfizer, New York, NY, USA) orally twice daily from day 1 to 14 each 14-day cycle. Surgery was planned for within 4 weeks after the last neoadjuvant toripalimab dose. Pathological complete response was defined as tumours without any viable tumour cells in the resected primary tumour sample and all sampled regional lymph nodes.

Primary tumor tissue and adjacent normal tissue, serum samples before and/or after ICI treatment, as well as paraffin-embedded formalin fixed (FFPE) slides prepared from enteroscopy biopsy and surgical samples were collected. The samples before ICI treatment were obtained after the initial diagnosis without immunotherapy, while the serum samples after ICI treatment were collected before

surgical resection, and the tissue samples after ICI treatment were from radical surgical resection. Overall, we collected 40 samples from 19 patients for single cell RNA profiling (See [Table S1](#) for details) and 74 serum samples from 27 patients for serum cytokine/chemokine quantification. In addition, we obtained 90 FFPE slides from 23 patients for multiplex immunofluorescence staining to verify the results of scRNA sequencing. Patients are all from the prospective PICC study and the expanded PICC study, 6 of which have participated in the scRNA sequencing in this study. In general, 90 samples were collected, of which 42 were - ICI (27 pCR, 15 non-pCR) and 48 were +ICI (38 pCR, 10 non-pCR). These samples were distributed into 4 panels for multiplex fluorescence immunohistochemical staining. All patients were provided written informed consent for the collection of tissue and blood samples for research and genomic profiling, as approved by The Sixth Affiliated Hospital of Sun Yat-sen University Review Board (#IRB 2021ZSLYEC-173).

In vivo mouse models

Male C57/BL6N mice aged 5–6 weeks were purchased from Jiangsu GemPharmatech and quarantined for one week before use. Animal care and experiments involved in this study were performed in accordance with Accreditation of Laboratory Animal Care International guidelines. Animal experiment protocols were approved by the guidelines established by the Animal Care Committee of the Sixth Affiliated Hospital, Sun Yat-sen University. 5×10^5 MC38 cells were suspended in 50 μ L of normal saline (NS) and subcutaneously injected. 500 μ g/kg IL1 β protein (HY-P7073A, MedChemExpress, USA) was intratumorally injected every day (five injections total). One day after the final injection, the tumor tissues were collected and analyzed by flow cytometry.

METHOD DETAILS

Sample collection and dissociation for scRNA-seq

All sample collection procedures complied with the regular routine in clinical practice. Tumor and adjacent normal samples were first stored in liquid nitrogen with the SenotechTM Tissue Storage Buffer (#JZ-SC-5802, Senotech Genomics, Shanghai, China) or proceed directly to tissue disassociation. The frozen tissue was heated in a 37°C water bath, and then was transferred to a new 15 mL centrifuge tube together with the frozen storage solution. 5 mL of preheated RPMI-1640 medium (GIBCO) was added to the centrifuge tube, which was further centrifuged at room temperature at 300 \times g for 5 min to remove the supernatant without disturbing the tissue sample at the bottom of the centrifuge tube. According to the manufacturer's protocol, the tissue samples were enzymolysis with Thermo Scientific at 37°C for 20–30 min. The isolated cells were then passed through a 40 mm cell filter (BD) containing 10% FBS in RPMI-1640 medium (Invitrogen) until a uniform cell suspension was obtained. Subsequently, the suspended cells were passed through a cell filter and centrifuged at 400 \times g for 10 min. Red blood cells were removed according to the manufacturer's instruction.

Single-cell RNA-seq library preparation and sequencing

Single-cell RNA-seq libraries were prepared using the Chromium Next GEM Single Cell 3' Kit from 10x Genomics, following the manufacturer's instructions. In brief, single cells were resuspended in PBS containing 0.04% BSA to a final concentration of 500–1,200 cells/mL as determined by Countess 3 Automated Cell Counters (Invitrogen). $\sim 10,000$ cells were captured in droplets to generate nanoliter-scale Gel bead in EMulsion (GEMs). GEMs were then reverse transcribed in a C1000 Touch Thermal Cycler (Bio-Rad) programmed at 53°C for 45 min, 85°C for 5 min, and held at 4°C. After reverse transcription and cell barcoding, emulsions were broken and cDNA was isolated and purified with Cleanup Mix containing DynaBeads and SPRIselect reagent (Thermo Fisher Scientific), followed by PCR amplification. Amplified cDNA was fragmented, end-repaired, double-sided size-selected, PCR-amplified with sample indexing primers, and subjected to library construction. Libraries prepared according to the manufacturer's user guide were then purified and profiled for quality assessment. Single-cell RNA libraries were sequenced by an Illumina NovaSeq 6000 or BGISEQ DNBSEQ-T7 sequencer with 150 bp paired-end reads.

Multiplex fluorescence immunohistochemistry

For multiplex fluorescence immunohistochemical staining, formalin-fixed and paraffin-embedded (FFPE) tumor tissue blocks were serially sectioned into 4–8 μ m sections. Multiplex immunofluorescence staining was conducted using the Akoya OPAL Polaris 7-Color Automation IHC kit (NEL871001KT) according to the manufacturer's protocol. Briefly, FFPE tissue slides were first deparaffinized in a BOND RX system (Leica Biosystems) and then incubated sequentially with primary antibodies CD4 (Abcam, Cat#ab133616, 1:100), FOXP3 (Abcam, Cat#ab20034, 1:100), CTLA4 (Abcam, Cat#ab237712, 1:500), TIM3 (Abcam, Cat#ab241332, 1:1000), CD68 (Abcam, Cat#ab213363, 1:1000), IL1B (NOVUS, Cat#NB600-633, 1:400), CD14 (Abcam, Cat#ab133335, 1:500), VEGFA (Abcam, Cat#ab1316, 1:600), MKI67 (CST, Cat#9449, 1:400), HLA-DR (Abcam, Cat#ab92511, 1:500), CD3 (Dako, Cat#A0452, 1:100), CD8 (Abcam, Cat#ab178089, 1:100), CD40 (Abcam, Cat#ab224639, 1:100), CD20 (Proteintech, Cat#60271-1-Ig, 1:400), CD68 (Zsbio, Cat#ZM0060, 1:500), CD163 (Zsbio, Cat#ZM0428, 1:100), PD-1 (Zsbio, Cat#ZM0381, 1:50) and PD-L1 (CST, Cat#13684, 1:100), CD8 (Zsbio, Cat#ZA-0508, clone SP16, 1:100) and CD57 (Zsbio, Cat#ZM0058, 1:100). This was followed by incubation with secondary antibodies (Vector Laboratories) and corresponding reactive Opal fluorophores. Nuclei acids were stained with DAPI (Akoya, Cat#210514003). Tissue slides that were bound with primary and secondary antibodies but not fluorophores were included as negative controls to assess autofluorescence. Multiplex stained slides were scanned using a Vectra Polaris Quantitative Pathology Imaging System (Akoya Biosciences) at 20 nm wavelength intervals from 440 nm to 780 nm with a fixed exposure time and an absolute magnification of $\times 200$. All scans for each slide were then superimposed to obtain a single image. Multilayer images were imported to inForm

v.2.4.8 (Akoya Biosciences) for quantitative image analysis. The quantities of various cell populations were expressed as the number of stained cells per square millimeter and further as the percentage of positively stained cells.

Luminex-based cytokine/chemokine detection for serum samples

Magnetic Luminex Assay kits were purchased from R&D Systems (catalog number: LKTM014). The tested cytokines/chemokines were as follows: CCL2 (MCP-1), CCL3 (MIP-1 α), CCL4 (MIP-1 β), CCL5 (RANTES), CCL11 (Eotaxin), CCL20 (MIP-3 α), CCL19 (MIP-3 β), CX3CL1 (Fractalkine), CXCL2 (GRO- β), CXCL10 (IP-10/GRO- α), IL-1 β , IL-1ra, IL-2, IL-4, IL-6, IL-7, IL-8, IL-10, IL-12 p70, IL-13, IL-15, IL-33, VEGF, PDGF-AA, PDGF-AB/BB, TGF- α , G-CSF, GM-CSF, PD-L1 (B7-H1), CD40 Ligand, FLT-3Ligand, IFN- α , IFN- γ , TNF- α , TRAIL, Granzyme B, and EGF. Serum samples cryopreserved at -80°C were thawed and analyzed according to the manufacturers' instructions. Data was acquired on a calibrated and validated Luminex MAGPIX instrument (R&D Systems, Abingdon, UK) as per manufacturer's instructions.

Tissue digestion and flow cytometry analysis for mouse samples

The tumor tissues for flow cytometry were cut into small pieces and digested with 1 mg/mL collagenase type IV (Sigma, USA; Cat#C5138) and 0.6 $\mu\text{g mL}^{-1}$ DNase (Sigma, USA; Cat#D5025) for 2.5h. Samples were then filtrated to single-cell suspension. Mouse 1 \times lymphocyte separation medium (DAKEWE, China; Cat#DKW33-R0100) was used to enrich tumor-infiltrating lymphocytes. Cells were stained with CD45-FITC (Biolegend, Cat#103108, 1:100), CD45-PE/Cyanine7(Biolegend, Cat#103114, 1:100), CD8-APC(Biolegend, Cat#100712, 1:50), PD1-Brilliant Violet 421(Biolegend, Cat#135218, 1:100), CD4-APC(Biolegend, Cat#100412, 1:100), CD25-PE (Biolegend, Cat#102008, 1:100), CD40-APC(Biolegend, Cat#124612, 1:100), CD19-Brilliant Violet 421(Biolegend, Cat#115549, 1:100). For intracellular staining, cells were proceeded with Foxp3/Transcription Factor Staining Buffer Set (eBioscience, Cat#00-5523-00) according to the manufacturers instruction and stained with FOXP3-Alexa Fluor 488(Biolegend, Cat#126406, 1:100). Subsequently, cells were analyzed by flow cytometry. The results were analyzed by CytExpert.

Serum cytokine/chemokine data analysis

Before Z score standardization of quantitative data (pg/mol), we set the value below the detection line to 0 and the value above the detection upper limit to the value of high concentration control. Normalized data were analyzed using R (version 4.1.0) software. Significant variations between the groups were analyzed using Wilcoxon test. p values of less than 0.05 were considered statistically significant.

Pre-processing of single cell RNA-seq data

Raw single-cell RNA-seq data were processed using 10X Genomics Cell Ranger toolkit (version 4.1.0), including demultiplexing the FASTQ reads, aligning them to the human reference genome (GRCh38, v3.0.0, from 10X Genomics), and generating the gene-cell unique molecular identifier (UMI) matrix (by using "cellranger count" function). Quality control and integration were performed using Seurat v4 R package.⁸⁰ We carried out several steps to filter out poor quality data. First, genes covered by less than 3 cells were filtered out. Then, all cells expressing <500 or >5,000 genes were removed, as well as cells that contained <400 or >25000 unique molecular identifiers (UMIs) to filter out the most of barcodes associated with empty partitions or doublet cells. On average, we detected 5,011 cells and 19,186 genes per sample after filtering. Cells with high mitochondrial gene expression are removed according to the broad cell type identified after batch effect correction and unsupervised clustering, as described below. To integrate and embed single cells from different individuals into a shared low-dimension space, we utilized integrated analysis (RPCA) by the Seurat v4 function "IntegrateData" to perform batch effect correction and normalization. The new integrated matrix was obtained and was used only for clustering and cell type classification.

Unsupervised clustering analysis and identification of broad cell type

After generation of the integrated matrix, we used an unsupervised graph-based clustering algorithm to cluster single cells by their expression implemented in Seurat v4.⁸⁰ The default parameters of Seurat were used, unless mentioned otherwise. Briefly, the UMI count matrix was normalized by using 'NormalizeData' function with default parameters. Based on the natural-log transformed normalized gene expression matrix, 2000 highly variable genes were generated using the 'FindVariableFeatures' function with the 'vst' method. For the clustering of all cell types, 2,000 variable genes were identified and 20 principal component analysis (PCA) was applied to the dataset to reduce dimensionality after regressing for the number of UMIs (counts). We used the function "FindClusters" on 20 PCs with resolution 1.2 to perform the first-round cluster and annotated each cluster by known markers (T cells: *CD3D*, *CD3E*, *TRAC*, *TRBC1*; B cells: *CD79A*, *CD79B*, *MS4A1*, *TNFRSF17*, *MZB1*; Myeloid cells: *CD14*, *CD68*; Epithelial cells: *EP-CAM*, *CD24*; Fibroblast: *COL1A2*, *COL3A1*, *MYH11*, *ACTA2*; Endothelial cells: *VWF*, *PECAM1*). Then cells with high expression level of mitochondrial genes in each cell type were then filter out, as described below. The remaining 155,397 cells were used to perform re-clustering using Seurat with the same parameters for visualization.

Removing cells with high expression level of mitochondrial genes

Furthermore, cells with unusually high detection rate of mitochondrial gene expression were excluded. Since mitochondrial RNA content are highly cell type dependent (notably higher in epithelial cells).⁸⁴ Thresholds were derived individually for cells within each compartment following an initial clustering. We first using several well-known markers to identify the cell types of the clusters and

combined the clusters belong to same cell type after removing extremely low abundance and conflicting clusters that co-express multiple broad markers (2.41%). Epithelial cells were removed if their proportions of mitochondrial gene expression were larger than 75% (29.75% of epithelial cells). Then, we fit the expression level of mitochondrial genes by using a median-centered median absolute deviation (MAD)-variance normal distribution,^{73,85} and then removed the cells with significantly higher expression levels than expected (determined by Bonferroni-corrected $p < 0.05$, 9.20% for lymphoid immune cells including T cells, B cells; 12.84% for myeloid cells; 8.11% for fibroblasts and 8.50% for endothelial cells). The remaining 155,397 cells were used to perform re-clustering using Seurat. As a result, high quality cells were clustered into 6 groups: epithelial cells, fibroblasts, endothelial cells, T cells, B cells and myeloid cells.

Dimensionality reduction using UMAP

For visualization, the dimensionality of each dataset was further reduced using the Uniform Manifold Approximation and Projection (UMAP) with Seurat functions “RunUMAP”. The PCs used to calculate the embedding were as the same as those used for clustering.

Re-clustering of broad cell types

Using T cell markers (*CD3D*, *CD3E*, *CD2*), we identified a total of 29,033 cells, which were annotated as T cells. Re-cluster analysis found that these T cells were mixed with NK cells. Clusters of cells with high mitochondrial gene expression and hybrid cells (10%) were excluded in the subsequent analysis. The remaining cells ($n = 25,986$) revealed well-defined subpopulations that were annotated based on published signatures, including the major T cell lineages ($CD4^+$ T cells and $CD8^+$ T cells) and three subsets of innate immune cells among including $\gamma\delta$ T cells expressing $\gamma\delta$ receptor genes (*TRDC*, *TRGC1* and *TRGC2*), NK cells with CD3 negative and overexpressed NK cell genes (*KLRD1*, *KLRC1*, *FCGR3A*, *TYROBP*), as well as a small amount of innate lymphocyte expressing *KIT*, and *KRT86*.⁸⁴ (Figure S2C, Table S2) In addition, proliferating T cells were shown as a mixture of $CD4^+$ and $CD8^+$ T cells. We further classified them according to the normalized expression of *CD4* and *CD8A* ($CD4$ Expr. $>$ $CD8A$ Expr., $CD4^+$ Prolif. T cells, $CD4$ Expr. \leq $CD8A$ Expr., $CD8^+$ Trm-mitotic cells).

Using B cell markers (*MS4A1*, *CD79A*, *CD79B*), we identified a total of 17,008 B cells to reveal 7 phenotypes after removing cells with high mitochondrial or ribosome gene expression (16%). Cells were first classified into plasma cells (*MZB1*, *XBP1*, *TNFRSF17A*, *IGHA1*, *IGHD1*) and $CD20^+$ B cells (*MS4A1*, *CD79A*, *CD79B*), and further annotated according to marker genes (Figure S2D, Table S2).

Using myeloid cell markers (*CD14*), we identified a total of 7,282 myeloid cells to reveal 10 clusters, including dendritic cell (DC) subsets, macrophage subsets and monocyte-like subsets (Figures S2E and S5A) after removing cells with high mitochondrial gene expression and hybrid cells (14%). DC subsets including plasmacytoid DCs (pDC , $LILR4A^+$ pDC), migratory DCs ($CCL19^+$ mDC) and conventional DCs ($CD1C^+$ cDC), which are characterized by high expression of HLA genes and low expression of *CD14*. Clusters were identified as macrophages based on their high expression of *CD68* or *CD163* and negative expression of monocyte markers (*FCN1*, *S100A8*, *S100A12*). Cells express monocyte signature genes (*FCN1*, *S100A8*, *S100A12*) without the expression of dendritic and macrophage markers were annotated as mono-like cells ($FCN1^+$ Mono, $IL1B^+$ Mono).

Using endothelial cell markers (*VWF*, *PECAM1*), we identified a total of 13,376 endothelial cells to reveal 6 phenotypes after removing hybrid cells (5.8%). Cells were classified into lymphatic endothelial cells (LEC) by expressing *LYVE1*, *CCL21*, *PROX1* genes and high endothelial venule (HEV) by expressing *MADCAM1*, *ACKR1* genes or annotated according to marker genes (Figure S2F). Using fibroblast cell markers (*COL1A2*, *COL3A1*, *MYH11*, *ACTA2*), we identified a total of 7,326 fibroblast cells to reveal three phenotypes after removing hybrid cells (7.7%). Cells were classified into myofibroblast by expressing *MYH11*, *ACTA2*, *MCAM*, *CAV1* genes or annotated according to marker genes (Figure S2G).

Identification of marker genes

To characterize each cluster, we applied the “FindAllMarkers” procedure in Seurat which identified markers using log fold changes (FC) of mean expression, and used Wilcoxon Rank-Sum test by default (min.pct = 0.25, logfc.threshold = 0.25). Marker gene list were show in Table S2.

Differential expression and functional annotation

Differential expression genes (DEGs) were identified using combination of “FindMarkers” function implemented in the Seurat package and pseudobulk method (‘Libra’ package).⁸⁶ Genes that met the criteria of adjusted P-value < 0.05 in Seurat method and P-value < 0.01 in pseudobulk method were considered as significant DEGs. Gene Ontology and pathway enrichment analyses of DEGs were performed using the ‘clusterProfiler’ R package.⁸⁷ Annotation Dbi R package “org.Hs.eg.db” was used to map gene identifiers. In each case, gene sets were tested for over-representation in cluster markers or DEGs by computing enrichment p values (‘enricher’ R function, default parameters) from the hypergeometric distribution. Hypergeometric p value was adjusted in each case for multiple testing using Benjamini-Hochberg correction. The results were visualized as bar plots using ‘clusterProfiler’ and ‘ggplot2’ R packages.

Definition of gene signature score

For computation of signature scores, average expression of the signature genes was counted based on the normalized matrix generated by Seurat Package. Cytotoxicity, exhaustion, and Treg score were defined by the average expression of published signature

gene according to the gene lists from Zheng et al.¹⁷ Proliferation score was defined by the average expression of known proliferation-related genes include *AURKA*, *BUB1*, *CCNB1*, *CCND1*, *CCNE1*, *DEK*, *E2F1*, *FEN1*, *FOXM1*, *H2AFZ*, *HMGB2*, *MCM2*, *MCM3*, *MCM4*, *MCM5*, *MCM6*, *MKI67*, *MYBL2*, *PCNA*, *PLK1*, *TOP2A*, *TYMS* and *ZWINT*.⁸⁸ Acute inflammatory response and chronic inflammatory response scores were defined by the average expression of genes annotated in “GOBP_CHRONIC_INFLAMMATORY_RESPONSE.v7.5.1 (GO:0002544)” and “GOBP_ACUTE_INFLAMMATORY_RESPONSE.v7.5.1 (GO:0002526)” from MSigDB gene sets.⁸⁹ Gene list to define CD8⁺ T cell signatures according to previous literatures were provided in [Table S3](#).

Gene set enrichment analysis

We used a fast per-ranked gene set enrichment analysis (GSEA) named fgsea (v1.18.0, R package)⁹¹ to perform functional enrichment analysis for defined gene signatures and previously reported gene signatures of cluster-specific DEGs (CD8 subset-A vs other CD8⁺ T cells, IL1B⁺ Mono vs other myeloid cells) and ICI treatment associated DEGs (+ICI/pCR vs -ICI, +ICI/non-pCR vs -ICI). First, DEGs were identified using the fast Wilcoxon rank sum test with ‘wilcoxauc’ functions implemented in ‘presto’ R package (<https://github.com/immunogenomics/presto>) and sorted according to AUC value, and then we fed each differentially expressed gene list together with AUC value of each gene and the gene sets to the ‘fgsea’ function (nperm = 1000). Gene sets with adjusted P value < 0.05 were selected as the functionally enriched biological states or processes. Positive normalized enrichment score (NES) means that a certain functional gene set is enriched in front of the sorting sequence, indicating upregulation in the specific cell population compared with other cells. While on the contrary, negative NES means certain functional gene set is enriched behind the sorting sequence, indicating down regulation in the specific cell population compared with other cells.

Correlation analysis

For single-cell based correlation analysis, we first calculated the cellular proportions of each immune cell cluster by their fractions in corresponding major immune compartments, which involve T/ILNK cell, B cell and myeloid cell compartments for each patient. We then evaluated the correlations of immune cell clusters by Pearson correlation test in the entire patient cohort (n=40).

Cell-to-cell communication of scRNA-seq data

We used CellChat (Version 1.1.3)⁹² to infer the cell-cell interactions across immune and stromal cell types using the expression of known ligand-receptor pairs. All databases curated in CellChatDB.human database including the “Secreted Signaling”, “Cell-Cell contact” and “ECM-Receptor” were included. Cells were annotated according to their cell type and sample groups: “-ICI”, “+ICI/pCR”, “+ICI/non-pCR”. To identify the changes of the cell-cell communication networks induced by ICI treatment in pCR response tumors, we followed the tutorial for comparison analysis of multiple datasets in the CellChat github repository (https://htmlpreview.github.io/?https://github.com/sqjin/CellChat/blob/master/tutorial/Comparison_analysis_of_multiple_datasets.html) and computed the major signaling changes between -ICI and +ICI/pCR groups by joint manifold learning and quantitative contrasts of multiple cell-cell communication networks. We compared the outgoing and incoming interaction strength of each pair of cell types to identify significant changes in sending or receiving signals between groups, and used the interaction strength to qualify the ICI treatment effect. We then visualized the most significant ligand-receptor pairs that mediate the cell-cell interaction changes across comparisons by using the netVisual_bubble function in CellChat.

Cell developmental trajectory

The cell lineage trajectory of CD8⁺ T and myeloid cells was inferred by using Monocle2.⁹³ We used the “differentialGeneTest” function to derive top 500 DEGs from each cluster and genes with a q-value < 0.05 were used to order the cells in pseudotime analysis. After the cell trajectories were constructed, differentially expressed genes along the pseudotime were detected using the “differentialGeneTest” function.

Cell subtype abundance estimated from TCGA bulk gene expression profiles

We integrated sc-RNA data and TCGA CRC bulk expression profiles to verify the correlation between cell subsets and functionalities in d-MMR/MSI-H CRC. We identified immune and stromal cell subtypes in human d-MMR/MSI-H CRC in this study ([Figure 1E](#)), and their specific gene signatures were derived marker genes of each subtypes identified using “FindAllMarkers” procedure in Seurat (Marker gene list were show in [Table S2](#)) based on following criteria: 1) FDR adjusted P-value < 0.05; 2) log2FC > 0.58. The TCGA-COAD and TCGA-READ data were used to evaluate the abundance of each cluster. The gene expression from these bulk RNA-seq datasets (‘HTSeq – FPKM’) were downloaded from TCGA data portal (<https://portal.gdc.cancer.gov/>). MSI classification results are derived from previously published study.⁹⁰ Subsequently, we estimated the relative abundance of each cell subtype by the average expression of Z score normalized log-transformed expression of the cell type specific genes defined above ([Table S4](#)).

Correlative cell-cell interactions inferred by combined scRNA-seq and TCGA MSI-H CRC datasets

To infer the correlative cell-cell interactions between immune cell subtypes by combined scRNA-seq and TCGA datasets, we applied methods from Zhang et al.³⁸ Briefly, cell subtype abundances were first estimated from TCGA MSI-H CRC bulk expression profiles as described above. Then we computed the Pearson correlation coefficient between the expression of each gene and the relative abundance of each cell subtype based on the bulk RNA-seq profiles and obtained a correlation matrix between genes and abundances of cell subtypes. Since the expression levels of certain signature genes in a given cell subtype were highly correlated

with the abundance of this specific cell subtype, we defined these genes as “self-expressed genes” based on our sc-RNA dataset according to the following criteria: 1) FDR adjusted p-value <0.05 ; 2) $\log_2FC > 0.58$; 3) cell frequency of expression $>35\%$. We then filtered these genes and transformed their correlation values to 0 to obtain an adjusted correlation matrix. Finally, for a specific cell subtype, to identify which cell subtypes could contribute to the highly correlated non-self-expressed genes, we performed a gene set enrichment analysis based on our sc-RNA dataset. In detail, we calculated the mean expression of each gene across each cell subtype and then performed Z score transformation. Next, the top 13 highly correlated non-self-expressed genes were selected from the adjusted correlation matrix. We then calculated the mean value of Z score transformed expression of these genes in each cell subtype as the enrichment score. Finally, the correlated cell subtype(s) was identified as the Z score transformed enrichment score >2.576 . The correlative networks were built separately with corresponding correlated cell subtypes (Figure S6F).

QUANTIFICATION AND STATISTICAL ANALYSIS

Statistical analyses were performed as described in Figure legends. Pearson correlation was used to estimate correlations among immune cell subsets. Statistical significance was determined by Kruskal-Wallis test, Wilcoxon test, Student T test and hypergeometrical test with the Benjamini-Hochberg method for multiple comparisons correction.